

COUPLED NON-PARAMETRIC SHAPE
AND MOMENT-BASED INTER-SHAPE POSE PRIORS
FOR MULTIPLE BASAL GANGLIA STRUCTURE
SEGMENTATION

by
MUSTAFA GÖKHAN UZUNBAŞ

Submitted to the Graduate School of Engineering and Natural Sciences
in partial fulfillment of
the requirements for the degree of
Master of Science
Sabancı University
August 2008

COUPLED NON-PARAMETRIC SHAPE
AND MOMENT-BASED INTER-SHAPE POSE PRIORS
FOR MULTIPLE BASAL GANGLIA STRUCTURE SEGMENTATION

APPROVED BY

Assist. Prof. Dr. Müjdat Çetin
(Thesis Supervisor)

Assist. Prof. Dr. Gözde Ünal
(Co-supervisor)

Assist. Prof. Dr. Hakan Erdoğan

Assoc. Prof. Dr. Mustafa Ünel

Prof. Dr. Aytül Erçil

Dr. Octavian Soldea (Substitute Member)

DATE OF APPROVAL:

©Mustafa Gökhan Uzunbaş 2008

All Rights Reserved

to all Electrical and Electronics Engineers
&
who are interested in brain image segmentation

Acknowledgments

I have been studying in Sabancı University since 2006. I have learnt a lot within these two years and gained many experience as an electronics engineer. The professors of vision and pattern analysis group in Sabancı University deserve a special thank.

First, I would like to express my appreciation to my advisor, Müjdat Çetin for his continuous guidance, suggestions, patience, and friendship during the course of my work. He guided me both as a mentor and as an academician. He has not only contributed tremendously to the technical content of this dissertation, but also provided a nice example of adviser-student relationship. I am very grateful to my professors Gözde Ünal and Aytül Erçil for their useful comments and eagerness to help. They provided very necessary feedback on this work and broadened my perspective with their constructive ideas. Additionally, I would like to thank Octavian Soldea, for sharing his all experience and knowledge with me. He has spent many hours with me and helped a lot while constructing 3D implementations.

I am also grateful to Assist. Prof. Hakan Erdoğan and Assoc. Prof. Mustafa Ünel for their participation in my thesis committee.

I would like to acknowledge The Scientific and Technical Research Council of Turkey (TÜBİTAK), for providing the financial support for my M.Sc.

Many thanks to my great colleagues, who always kept my motivation high and refreshed my mana. I am fortunate and indebted to my friends with whom I shared a considerable portion of my daily life.

I am grateful to my parents for their everlasting trust, encouragement, emotional support, and pure love. I thank my mom, dad, and sister for supporting my decision to spend this many years away from them. Finally, I would like to express my deepest gratitude to my respected and most beloved girl friend Gizem Karşlı who helped me to pursue my ambitions and career and always supported, encouraged and loved me. This work could not have been completed without her unconditional love and support.

COUPLED NON-PARAMETRIC SHAPE
AND MOMENT-BASED INTER-SHAPE POSE PRIORS
FOR MULTIPLE BASAL GANGLIA STRUCTURE SEGMENTATION

MUSTAFA GÖKHAN UZUNBAŞ

EECS, M.Sc. Thesis, 2008

Thesis Supervisor: Assist. Prof. Dr. Müjdat Çetin

Thesis Co-Supervisor: Assist. Prof. Dr. Gözde Ünal

Keywords: multiple brain structures segmentation, coupled shape priors, pose prior, active contours

Abstract

Brain tissue and structure segmentation in magnetic resonance (MR) images is a fundamental problem in clinical studies of brain structure and function. Due to limitations such as low contrast, partial volume effects, and field inhomogeneities, the delineation of subcortical (basal ganglia) structures such as caudate nucleus, putamen, and thalamus from white matter, gray matter and cerebrospinal fluid (CSF) is a very challenging problem.

This thesis presents a new method for simultaneous segmentation of multiple brain structures. We formulate the segmentation problem as a maximum a posteriori estimation problem, in which we incorporate statistical prior models on the shapes and relative poses of the structures of interest. Our method is motivated by the observation that neighboring or coupling structures in medical images generate configurations and co-dependencies which could potentially aid in segmentation if properly exploited. Our coupled shape priors are learned through nonparametric multivariate kernel density estimation based on training data. Relative pose priors are modeled via standard moments. Given this framework, the segmentation problem turns into an optimization problem, which we solve using active contours. We present experimental results on synthetic data as well as on a rich set of real MR

images demonstrating the effectiveness of the proposed method in segmenting basal ganglia structures as well as improvements it provides over existing approaches.

PARAMETRİK OLMAYAN BAĞLAŞIK ŞEKİL VE ORTAK POZİSYON BİLGİSİ
TABANLI BİR YÖNTEM İLE BEYİN KORTEKS ALTİ YAPILARIN BÖLÜTLENMESİ

MUSTAFA GÖKHAN UZUNBAŞ

EECS, Master Tezi, 2008

Tez Danismani: Yard. Doc. Müjdat Çetin

Tez Yan Danismani: Yard. Doc. Gözde Ünal

Özet

Beyin manyetik rezonans görüntülerinde beyin dokularının ve yapılarının bölütlenmesi klinik uygulamalarda temel bir problemdir. Özellikle beyindeki beyaz madde, gri madde ve beyin öz sıvısı içerisinde gömülü halde bulunan Putamen, Kaudat, Talamus gibi korteks altı yapıların ayrıştırılması oldukça zordur. Bu zorlugun nedeni, manyetik görüntülerde bu dokuların düşük kontrastlı görülebilmesi, homojen olmayan yoğunluğa sahip olması ve kısmi hacim etkilerinin olmasıdır.

Bu tezde bahsedilen çoklu beyin yapılarının aynı anda bölütlenmesi için yeni bir yöntem geliştirilmiştir. Bölütleme problemi en büyük sonsal kestirim çerçevesinde oluşturulmuş ve bu çerçevede hedef yapıların istatistiksel şekil önsel bilgisi ve göreceli poz modelleri bölütleme işlemine katılmıştır. Bu yöntemimiz medikal imgelerde sıklıkla rastlanan birbirine komşu, çoklu yapıların belirgin kombinasyonlar ve ortak bağlaşıklıklar yaratmasından esinlenerek geliştirilmiştir. Buna göre eğer bu bağımlılık ve kombinasyonlar doğru şekilde modellenenirse, bölütlenmesi zor yapıların bölütleme başarımını artıracakını öne sürmekteyiz. Onerimizde bağlaşıklık şekil ön bilgisini parametrik olmayan çok değişkenli Parzen yoğunluk kestirimi kullanarak oluşturmaktayız. Bunun için bölütlemek istediğimiz yapıların eğitim kümesinden faydalanırız. Göreceli pozisyon bilgisini ise standart moment teorisi ile modelleriz. Bu çerçevede her iki önsel bilgiyi de bölütlemeye katarken problemi bir optimizasyon problemi olarak ele alırız ve çözümünde etkin çevritlere dayalı bir yöntem kullanırız. Yöntemin başarımını sentetik ve pek çok gerçek beyin manyetik rezonans görüntüsü üzerinde göstermekteyiz. Sonuçları var olan diğer yöntemlerle de karşılatırmakta ve

üstün yönlerini belirtmekteyiz.

Table of Contents

Acknowledgments	v
Abstract	vi
Özet	viii
1 Introduction	1
1.1 MR Image Segmentation Problem	3
1.2 Main Contributions	6
1.3 Organization	8
2 Background	9
2.1 Active Contour Based Image Segmentation	9
2.1.1 Energy Minimization and Speed Function Definition	15
2.1.2 Level Set Representation and Curve Evolution	16
2.2 Nonparametric Density Estimation	19
2.3 Shape and Pose Analysis	20
2.3.1 Shape Representation and Space of Shapes	21
3 Segmentation Based on Shape and Pose Priors	24
3.1 Motivation for Coupled Shape and Inter Shape Pose Priors	24
3.2 Segmentation Framework by Energy Minimization Based on Curve Evolution	25
3.2.1 Coupled Shape Prior for Multiple Objects	28
3.2.2 Moment-based Relative Pose Prior for Multiple Objects	30
3.3 Segmentation Algorithm	32
4 Experimental Results	35
4.1 Synthetic Data	36
4.2 Real Data	38
5 Conclusion	46
5.1 Summary	46
5.2 Future Work	47
Bibliography	49

A	Analytical Computation of Coupled Shape Prior Flow	56
A.1	Derivation of the Coupled Shape Prior Evolution Formula	56
A.2	Coupling Effect of Multiple Shapes	58
B	Analytical Computation of Inter-Shape Pose Prior Flow	59
B.1	Derivation of the Inter-Shape Pose Prior Evolution Formula	59

List of Figures

1.1	Magnetic Resonance Imaging Machine Cutaway [1]	2
1.2	MRI data taken from axial section in proton density sequence and its volumetric presentation.	3
3.1	Alignment of training shapes for Nucleus Caudate (NC) and Putamen (P). (a) superposition of unaligned binary shapes of multiple objects (NC + P), (b) superposition of globally aligned binary shapes of multiple objects (NC + P) (c) superposition of locally aligned binary NC shapes, (d) superposition of locally aligned binary P shapes . . .	27
3.2	Moments based inter-shape pose reconstruction. The small white circles are the mass centers of the corresponding objects. The green small circles are the mass centers of the blue and red objects together. (a) initialization, (b) iteration 140, (c) steady state after iteration 200.	31
3.3	Segmentation Algorithm - In each step, three forces are evaluated: C&V, Coupled Shape (see Section 3.2.1), and Inter-Shape Pose (see Section 3.2.2)	34
4.1	A picture of interface that is used for manual segmentation.	36
4.2	Segmentations on synthetic data. (a) C&V method, (b) single shape [32], (c) inter-shape pose only, (d) proposed coupled shape and inter-shape pose priors.	37
4.3	Segmentation results of the CN and the P in an MR slice: (First column) C&V method, (Second column) single shape prior only (Putamen), (Third column) single shape prior only (head of Caudate), (Forth Column) proposed coupled shape prior.	42

4.4	Segmentation results of the left part of the CN and the P in an MR slice: (a) C&V method, (b) single shape prior only (see [32]), c) inter-shape pose prior only, (d) proposed coupled shape and inter-shape pose prior.	43
4.5	Segmentation results of the CN and the P in an MR slice: (First column) C&V method (see [18]), (Second and Third column) single shape prior, (Forth column) proposed coupled shape prior only, (Fifth column) proposed coupled shape and inter-shape pose prior.	44
4.6	3D segmentation: (a) Volumetric representation of target structures, segmentation results of the CN and the P in an MR volume (b) Using only ChanVese, (c) Using coupled shape prior	45

List of Tables

3.1	Area and mass center distance (MCD) reconstruction measurements in pixels. MCD is the distance between the white (corresponding) mass center and the green one in pixels.	32
4.1	Average quantitative accuracy results for the experiment shown in figure 4.2	37
4.2	Average quantitative accuracy results for the experiments in figure 4.3	39
4.3	Quantitative accuracy results for the experiments in figure 4.2.	39
4.4	Average quantitative accuracy results for the experiments in figure 4.5	40

Chapter 1

Introduction

Medical imaging is an important source of anatomical and functional information and it is necessary for the diagnosis and treatment of diseases. The advent of medical imaging modalities such as X-ray, ultrasound, computed tomography (CT) and magnetic resonance imaging (MRI) has greatly improved the diagnosis of various human diseases. In the last two decades, computer-aided medical image analysis techniques have been employed to provide a better insight into the obtained image data. With the recent developments, medical image analysis community has become interested in many challenging problems of creating algorithms. According to the developments, the primary tasks of medical image analysis in this field are; image segmentation, registration, and matching. Such techniques provide better insight about the patient condition and allows for more accurate, shortcut diagnosis methods. Computerized applications like image data fusion, quantitative analysis, generating anatomical atlases, 3D visualization are very hot topics which helps for better diagnosis and treatments.

Medical images can also be analyzed for examining relationships between structural abnormalities and deformations and certain functional abnormalities and diseases. Many computer-based methods are used to define the detailed shape and organization of anatomic structures for more accurate and faster treatments. In this context, in recent years, image analysis on MR images has become popular. In particular, MRI has become a leading technique widely used for imaging soft brain tissue. MR images are generated by measuring the behaviour of soft tissue under a magnetic field. In an MR image different tissues give different intensities. From the brain MRI perspective it provides better resolution and contrast according to other

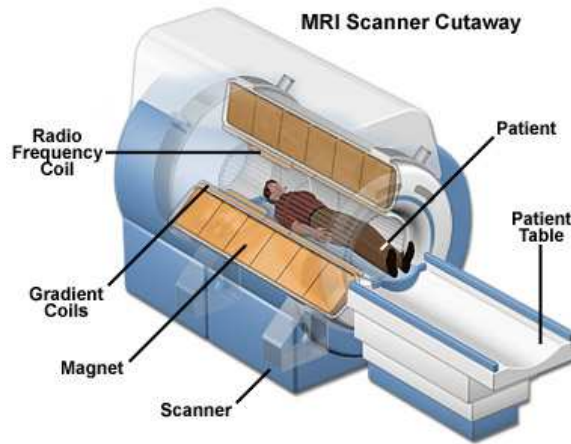


Figure 1.1: Magnetic Resonance Imaging Machine Cutaway [1]

modalities.

Focusing on brain studies, quantitative morphologic assessment of individual brain structures in neuro-imaging most often includes segmentation. Medical image segmentation is the most important step in visualization, surgical guidance and planning, diagnosis and quantitative measurement [2]. It can provide information about both the location and the anatomical structure of internal organs and parts of the human body, thereby assisting medical diagnosis and therapy evaluation. Detailed segmentation and subsequent 3D models can be used to generate an anatomical atlas for visualization and learning. A fully segmented scan allows surgeons to both better qualitatively visualize the shapes and relative positions of internal structures and more accurately measure their volumes and distances quantitatively. Segmentation tools can be also used to analyze for examining relationships between structural abnormalities and deformations and certain functional abnormalities and diseases. For example, segmentation of subcortical structures in brain MR images is motivated by a number of medical developments including the early diagnosis of neurodegenerative illnesses such as schizophrenia, Parkinson's, and Alzheimer's diseases. In this context, the analysis of chemicals in Basal Ganglia (BG) structures is thought to provide important cues [3]. Scans of people without pathological abnormalities can be used as a method for comparison to define abnormality. However, their accurate segmentation remains a challenging task in the clinical environment.

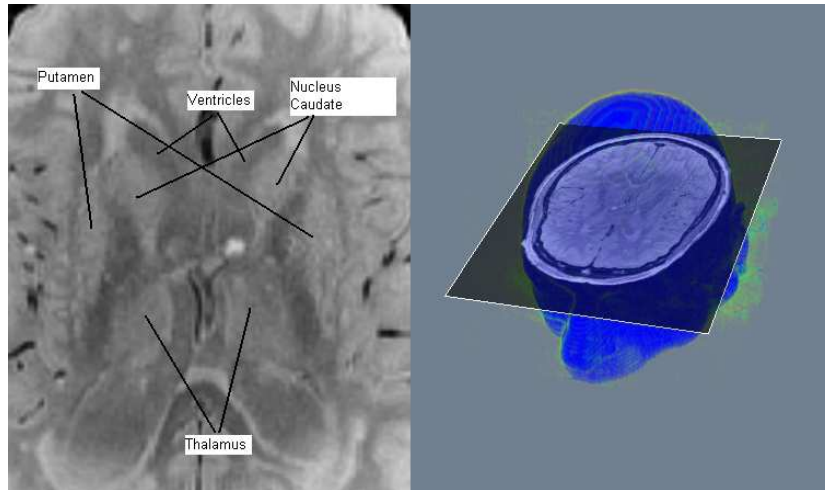


Figure 1.2: MRI data taken from axial section in proton density sequence and its volumetric presentation.

1.1 MR Image Segmentation Problem

Brain tissue segmentation in MR images is a fundamental problem in clinical studies of brain structure and function. Some examples of such studies deal with measures of tissue/structure volumes, voxel-based morphometry, etc. Segmenting an anatomical structure in an MR image amounts to identifying the region or boundary in the image corresponding to the desired structure. However, efficient computer-assisted segmentation of internal anatomy that produce accurate results is limited since many important structures in MR images do not present a clear boundary for segmentation and have variations between different subjects. The relative contrast between brain tissues is not constant in MR imaging. In most medical imaging applications, little can be done about the appearance of anatomically distinct areas relative to their surroundings. The choice of the strength and timing of the radio-frequency pulses, known as the MRI sequence [4], can be employed to highlight some type of tissue according to the clinical application. However, due to the limitations such as low signal-to-noise ratio (SNR), partial volume effects, and field inhomogeneities the delineation of subcortical regions like caudate, putamen, thalamus, etc. from white matter (WM), gray matter (GM) and cerebrospinal fluid (CSF) is very difficult [5], see Figure 1.2.

Motivated by these facts, most segmentation applications still require at least

some amount of manual intervention and some are performed completely manually. However, manual segmentation is tedious, time consuming and also not reproducible. To compensate these drawbacks and make automated clinical segmentation tools, there have been many methods proposed for brain tissues in the subcortical regions [6], [7], [8], but they still remain challenging tasks.

A great amount of research was performed during the past three decades toward complete automated solutions for general-purpose image segmentation. Variational techniques [9], [10], statistical methods [11], [12], combinatorial approaches [13], curve-propagation techniques [14], and methods that perform non-parametric clustering [15] are some examples.

In the curve-propagation approaches, general idea is that an initial curve estimate of the structure boundary is provided and optimization methods are used to refine the initial estimate based on image data. This approach, called active contour models, is based on the optimization of an energy functional using partial differential equations. In the definition of the energy functional, earlier methods use the boundary information for the structures of interest [16], [14], [17]. More recent methods use regional information such as intensity statistics like mean or variance of an area [18], [19], [20]. In most recent active contour models, a shape prior model is used where richer models generate more accurate results. In these approaches several shape representation methods are used in the literature that are based on distance functions, implicit representations, and relationships among different shapes, including pose, orientation, and other geometrical relations [21], [22]. In [23], the authors present an active contour segmentation method based on (Legendre) moments analysis towards building a shape prior. From subcortical structure segmentation perspective, typical approaches rely heavily on prior information which is obtained from training data. The information might be in the form of tissue probability maps (probabilistic atlases) [24] or shape priors [21], [25], [26], [27], [28], [29]. The class of approaches using probabilistic atlas priors [24] rely on the accuracy of the manual segmentations of subcortical structures in the training data that generates the probabilistic atlas. Here, the accuracy of the registration method should also be reliable to map the template space to the subject space, in the absence of strong intensity contrast in the subcortical tissues.

Most recent methods benefit from knowledge about the structures of interest. This makes the segmentation process robust to the imperfect image conditions. There are numerous existing automatic segmentation methods that enforce constraints on the underlying shapes. In [21] the authors introduce a mathematical formulation to constrain an implicit surface to follow global shape consistency while preserving its ability to capture local deformations. Closely related with [21], in [25] [26], modeling consists of an average shape and modes of variation through principal component analysis (PCA) which is used to capture the variability of shapes. However, this technique can handle only unimodal, Gaussian-like shape densities. In [25], the image term and prior term are well separated where prior knowledge and data fidelity are imposed into segmentation in a MAP (Maximum a Posteriori) criterion . In [26] a region-driven statistical measure is used to define the image component of the function while prior term refers to the projection of the contour to the model space using a global transformation and a linear combination of the basic modes of variation. In [27], [28], [29] shape model refers only to an average shape in an implicit form and the prior term refers to the projection of the evolving contour to this space according to a similarity transformation.

As an alternative solution to PCA limitations, [30] proposes a principal geodesic analysis (PGA) model. In this context, [31] proves the applicability of PGA to medical images analysis. As a solution to the limitation of PCA and unimodal Gaussian distribution models, techniques based on nonparametric shape densities learned from training shapes have been proposed in [10] [32]. In those works, it is assumed that the training shapes are drawn from an unknown shape distribution and this distribution is estimated by extending a Parzen density estimator to the space of shapes. They formulate the segmentation problem as a MAP estimation problem, where they use a nonparametric shape prior. In particular, one theory is to construct the prior information in terms of a shape prior distribution such that for a given arbitrary shape we can evaluate the likelihood of observing this shape among shapes of a certain category (e.g. the Caudate Nucleus).

Although nonparametric priors are adequate to capture non-linear shape variability, until now they have not been used in multi-object segmentation techniques where there is superior potential in achieving accurate segmentation, if they can

model the inter-shape relationships among the components. The anatomical structures in the brain are related to the neighboring structures through their location, size, orientation, and shape. In many cases, objects to be segmented, have one or more neighboring structures. An integration of these relations into the segmentation process can improve the accuracy and robustness [33], [34], [35]. Very little work has been presented toward the automatic simultaneous detection and segmentation of multiple organs. In [33], a joint prior based on a parametric shape model, is proposed to capture co-variations shared among the different shape classes, which improves the performance of segmentation. With a similar approach in a Bayesian framework, in [35], [34] joint prior information of the multiple objects is used to capture the dependencies among the different shapes where multiple objects with clearer boundaries are used as reference objects to provide constraints in the segmentation of poorly contrasted objects. Another coupled shape prior model, which is based on the cumulative distribution function of shape features, is proposed in [36]. In [36], relative inter-object distances are defined as a shape feature to capture information about the interaction between multiple objects. Among spatial dependencies between multiple structures, one basic aspect is inter-shape pose analysis [37]. Clinical applications support a statistical shape modeling of multi-object group rather than one of single structures outside of their multi-object context. Neighboring anatomical shapes usually exhibit strong mutual spatial dependencies [31]. In this context, [38] proposes a solution for the segmentation problem in the presence of hierarchy of ordered spatial structures. In [39] the authors present progress towards modeling the shape and pose variability of sets of multiple objects. They use principal geodesic analysis (PGA) which is the extension of the standard technique of principal component analysis (PCA) into the nonlinear Riemannian space. Therefore, inter-shape pose analysis is a challenging problem, which aims augmenting segmentation algorithms.

1.2 Main Contributions

In this section we introduce the contributions of the thesis to the field of active contour models for medical image segmentation. The paragraphs below present our work in a general context and point to different chapters within the thesis where the

reader can find detailed information about specific contributions. Note that minor overlap in the chapters may be noticed since they were written to be self-contained. We propose a new multi-object segmentation scheme that introduces nonparametric *coupled* shape and *inter-shape* pose priors. Our multi object, coupled shape prior computation is closely related with [32] and [10] where nonparametric density estimate of single object shape is computed. We use multivariate Parzen density estimation to estimate the unknown density of multiple subcortical structures in the brain. Different from other multi object segmentation methods, our model provides coupling effect in a very natural and easy way. Motivated by the fact that, inter-shape pose analysis provides strong mutual dependencies between subcortical structures we introduce inter-shape pose prior into segmentation with shape prior in the same framework. We propose that our relative pose prior is a strong force that attracts the active contours to evolve toward more accurate segmentation. In this context, we define two probability densities in the space of shapes and pose by modeling the statistical prior information of the analyzed objects. Both of the densities are evaluated during the evolution of active-contours, aiming an energy functional minimization.

To the best of our knowledge, our approach is the first scheme of multi-object segmentation, which employs coupled shape and inter-shape pose priors based on moment computations in a probabilistic framework. We present experiments on synthetic and real MR images accompanied by quantitative analyses of the segmentation accuracy.

For coupled shape priors, we propose nonparametric density estimates based on signed distance functions (SDF) of training shapes. This key property of our method allows segmenting multiple objects simultaneously where the new prior provides automated, coupled constraints to be used in challenging image scenarios. Moreover, as compared to existing methods [33], [35] which are based on prior of multiple objects, our approach has the advantage of using nonparametric density estimate, in order to capture non-linear shape variability.

For inter-shape pose priors, we use standard moments, which are intrinsic to shape and have natural physical interpretations [40]. Standard moments describe, among other pose parameters, the size, the mass center, and the orientation of

the analyzed objects' SDFs. In addition, moments evaluation is computationally attractive.

1.3 Organization

This paper is organized as follows. Chapter 2 provides the background and context that underlie the work described in subsequent chapters. It begins with a brief review of key pieces of work in the development of active contour models and some previous work on shape and pose analysis. Chapter 3 presents our coupled shape and inter-shape pose prior based multi object segmentation method. Chapter 4 presents experimental results for subcortical structures on synthetic and real MR images with validation consequences. In chapter 5 we conclude by summarizing the contributions of this paper. We also suggest some possible extensions and future research directions.

Chapter 2

Background

In this chapter, we provide background material relevant to the development of the material in later chapters. In Section 2.1, we briefly review key pieces of work in the development of active contours and discuss some related work on image segmentation. Section 2.1.1 provides preliminary information on energy minimization and gradient flow, which are used in the implementation of active contours. Section 2.1.2 also presents level set formulation and curve evolution theory based on signed distance functions. In section 2.2, we review nonparametric density estimation in shape spaces. In particular, section 2.2 provides formulation for nonparametric density estimation of multiple random variables. In Section 2.3, we review previous work on shape and inter-shape pose analysis. Section 2.3.1 reviews the topic of shape prior based segmentation. Section 2.3.1 provides preliminary information on moment theory, which is used to extract geometric features of shapes.

2.1 Active Contour Based Image Segmentation

Deformable models pioneered by Kass et al. [14], are in general, curves or surfaces that move under the influence of internal and external image forces. The approach in [14] represents the boundary between regions as a closed contour and the contour is evolved until it converges to the boundaries of objects. The evolution process corresponds to an iterative optimization of a variational cost functional. In the literature there are two major classes of deformable models. The first one is parametric, point based models through which the contour is represented explicitly. The second one is implicit models that represent the surface implicitly as the level set of a higher

dimensional scalar function [41].

In explicit representation the contour or the surface is represented by a finite set of parameters, eg. the spatial positions of points on the curve are used to reconstruct the evolving surface by connecting them with line segments in 2D as in polygons and in three dimensions, as polyhedrals [42]. One difficulty of this approach is keeping connectivity of the points on the surface which are very likely to change during the evolution. Another consideration is that, the discretization should be fine enough to reconstruct the surface. Moreover, if the points come too close together, they may cross each other if the time step is not adjusted properly. A solution for such problems is to redistribute the points every few time steps, and add or remove points where this is necessary. However, this task becomes complicated, especially in three dimensions. A more serious problem arises in the presence of a change in the topology. Generally, the parametric approach is not capable of handling topology changes, unless special constraints are implemented for detecting possible splitting and merging of contours [41].

The difficulties in parametric models bring us to one of the main advantages of level set methods since they represent the interface implicitly. Level sets can handle topology changes naturally and automatically in any dimension where parametric models require modification in representation for different dimensions. The level set method works equally well in any dimension. For these reasons, active contour models based on level set methods have received considerable attention, and the evolution method in our thesis also depends on level sets.

The evolution of the deformable models is derived in an energy minimization process. The energy functional is composed of several internal and external potential forces. Different approaches have been proposed to construct such energy functionals. According to the definition of the external forces, active contour based segmentation methods are classified into 2 major classes: edge (boundary) based and region based methods. In the earlier development of deformable models, boundary based methods have been introduced first. Boundary based methods primarily use edge information to attract the snake to boundaries with large image gradients (strong edge locations). Initially introduced by Kass et al. [14], the energy functional to be minimized is composed of two smoothness terms for the contour and

one external energy that attracts the contour toward edges, which are points of high intensity gradient. The energy functional is given by

$$E_1(C) = \alpha \int_0^1 \|C'(s)\|^2 ds + \beta \int_0^1 \|C''(s)\|^2 ds + \gamma \int_0^1 \|\nabla I(C(s))\| ds \quad (2.1)$$

where α, β, γ are corresponding weighting coefficients for each energy term. Here, s corresponds to $(x(s), y(s))$ and $C(s)$ is the evolving curve parameterized with spatial coordinate s , and I is the image intensity. In this approach, such reliance on edge information, makes the model sensitive to image noise and to various other image artifacts. For example, the contour may get stuck in local minima due to strong edges inside or outside the object's true boundary. The drawback of this method is that it requires a good initial curve for accurate segmentation [43].

The level set based models proposed by Caselles et al. [16], called geodesic active contours, and by Yezzi et al. [44], called geometric active contours, drive the curve in the normal direction of contour curvature attracted with an edge indicator function.

$$E_2(C) = \int_0^1 g(I(C(s))) ds \quad (2.2)$$

Here, the edge indicator function $g(\cdot)$ is given as

$$g(I) = \frac{1}{1 + \|\nabla(G_\sigma(s) * I(s))\|^2} \quad (2.3)$$

where $G_\sigma(s) * I(s)$ is the convolution of the image with a Gaussian filter. The edge indicator function becomes smaller as the gradient gets larger. In this case it behaves as a stopping function. A drawback of this approach is that if the boundary does not provide high gradient the contour passes through the boundary. The stopping function may not become small enough to stop the evolution. Moreover, in the presence of high noise even if we have significant smoothing to prevent detection of false boundaries it increases the probability of missing edges.

To address these limitations there have been significant efforts in the literature to integrate region information into deformable models. In general, region based deformable models drive the contour or surface according to the first and second

order intensity statistics. Initial region based methods rely on the homogeneity of spatial features such as gray level intensity and texture. The advantage of such methods according to edge based methods, is that since they rely more globally on the gray level image, they are less susceptible to noise than methods that use derivative information. In particular, the methods we will consider in this section are generally based on Mumford-Shah functional which has emerged before the active contour framework [9]. The original Mumford-Shah functional is given as follows

$$E(f, C) = \int_{\Omega} (f - I)^2 ds + \gamma \int_{\Omega - C} \|\nabla f\|^2 ds + \alpha \|C\| \quad (2.4)$$

In this equation, in image domain Ω , I is the image intensity observed and f is the piecewise smooth approximation of the observed image. $\|C\|$ stands for the total length of the curve. The idea is to minimize the difference between I and f with the constraints of the curve smoothness and curve length. It has then been formulated in an active contour framework [18] [45]. In [18], a model can be obtained which can detect contours both with or without gradient i.e., objects with smooth boundaries or with discontinuous boundaries. In [18], the image is assumed to be formed of two regions of piecewise constant intensities of distinct values. In the energy functional a fitting term is defined and this fitting term is composed of differences between mean intensity values and observed intensities inside and outside the segmenting curve.

$$E_3(C) = \int_{in(C)} (I(s) - c_1)^2 ds + \int_{out(C)} (I(s) - c_2)^2 ds \quad (2.5)$$

where $in(C)$ and $out(C)$ represent the interior and exterior of C , respectively.

The fitting term provides maximizing the difference of mean intensities in the region, outside and inside the contour. This method essentially takes the mean intensity of each region as the discriminative statistical feature for segmentation. In the equation above, c_1 and c_2 are mean intensity values inside and outside the contour. Higher order statistics rather than the mean and the variance were utilized in [46] to account for textural characteristics of regions in images.

Both edge and region based deformable models often suffer from a variety of limitations. In the presence of noise, distortion or assimilation with the background, segmentation becomes challenging. In these cases, object boundaries do not fully

correspond to edges in the image and may not delimit homogeneous image regions. To improve the accuracy of segmentation results, methods that integrate edge and region based information have been proposed in several works [47], [48], [49], [50]. In [51], the method uses Green’s theorem to derive the boundary of a homogeneous region-classified area in the image and integrates this with a gray level gradient based boundary finder as seen in the equation below:

$$E_4(C) = \alpha \int_C g(I(C(s)))ds + \beta \int_C I(C(s))ds \quad (2.6)$$

These image segmentation problems demand the incorporation of as much prior information as possible to help the segmentation algorithms extract the region of interest. In curve evolution methods, a penalty on the length of the segmenting curves is often used as a simple shape prior for the objects in the scene. However, in many applications, more information is available regarding the shapes of the objects. There are numerous existing active contour segmentation methods that enforce constraints on the underlying shapes [47], [52], [25], [10], [32], [36]. In [52], the authors find a set of points across a set of training images to construct a statistical model of shape variation which is then used in the localization of the boundary. In [25], principal component analysis (PCA) is used to capture the variability of shapes. They add an energy term to the geodesic active contour model to pull the surface in the direction of the MAP shape. It is given by

$$\begin{aligned} E_5(C) &= -\log P(\alpha, p|C, \nabla I) \\ &= -\log P(C|\alpha, p) - \log P(\nabla I|\alpha, p, C) \\ &\quad - \log P(\alpha) - \log P(p) \end{aligned} \quad (2.7)$$

The first term computes the probability of a certain curve C given the shape and pose of the final curve α, p . The second term computes the probability of seeing certain image gradients given the current and final curve. The last two terms are based on shape and pose priors. They assume pose prior as uniform. The authors evolve an active contour both locally, based on image gradient and curvature, and globally to the MAP estimate of shape and pose. However, this technique can handle only unimodal, Gaussian-like shape densities.

In a more challenging approach in [21], the authors proposed a method in which they generate a shape model that can account for local variations as well. To compensate the dependency of PCA based methods they consider a stochastic framework which includes shape image and local degrees of shape deformations. They describe each grid location in the shape model using Gaussian density function as

$$p_{x,y}^M(\phi) = \frac{1}{\sqrt{2\pi}\sigma_M(x,y)} e^{-\frac{\phi - \phi_M(x,y)}{2\sigma_M^2(x,y)}} \quad (2.8)$$

where $\phi_M(x, y)$ is model binary shape image and $\sigma_M(x, y)$ is local degree of shape deformation. Given N aligned training samples where $\tilde{\phi}_i$ is the aligned transformation of ϕ_i , they construct a variational framework for the estimation of the best shape by searching for the maximum likelihood of the local densities. They propose a cost functional with respect to (ϕ_M, σ_M) as

$$E(\phi_M, \sigma_M) = - \sum_{i=1}^n \int \int [p_{x,y}^M(\tilde{\phi}_i(x, y))] dx dy \quad (2.9)$$

Techniques based on nonparametric shape densities learned from training shapes have been proposed in [10], [32]. In those works, it is assumed that the training shapes are drawn from an unknown shape distribution and this distribution is estimated by extending a Parzen density estimator to the space of shapes. They construct the energy functional both using region statistics like mean and variance, and shape distribution term.

$$E_6(C) = -\log P(\text{data}|C) - \log P(C) \quad (2.10)$$

In this Bayesian approach, first term at right hand side is the likelihood function which provides data fidelity. It is computed as in [18], which is based on regional intensity statistics and evolves the curve in order to catch smooth, unclear boundaries. The second term, the shape prior, is based on a set of shapes. Using a training set, the authors compute the unknown distribution of the shapes and use this prior as a regularizer in the active contour cost functional. They compute the shape distribution in a nonparametric way such that it brings the advantage of an ability to catch nonlinear shape variability.

Simultaneous multiple object segmentation is an important direction of research such that the positions of segmented parts are often highly correlated and can be

used to further constrain the resulting boundary estimation. In [36], relative inter-object distances are defined as a shape feature to capture information about the interaction between multiple objects. The energy functional consists of a data term and a shape prior term which is based on the shape distributions composed of shape features.

$$E_7(C) = E_{data}(C) + \alpha E_{prior}(C) \quad (2.11)$$

The data term $E_{data}(C)$ favors the fidelity of the solution to the data. This term is application specific. $E_{prior}(C)$ reflects the information about shape and parameter that weighs the strength of the prior. They introduce the formulation of the shape prior in the continuous domain as

$$E_{prior}(C) = \sum_{i=1}^M w_i \int \left(\tilde{H}_i(\lambda) - H_i(C, \lambda) \right)^2 d\lambda \quad (2.12)$$

Here M is the number of feature classes taken into account, $\tilde{H}_i(\lambda)$ is the target distribution function of the i^{th} feature class, $H_i(C, \lambda)$ is the distribution function of the i^{th} feature class for the curve C and w_i is the weighting coefficient for each feature class. λ is a variable spanning the range values of the feature. They provide 3 feature classes: inter node distances of the discrete curve, multiscale curvature, and finally relative inter-object distances. This 3rd feature class encodes the relative position of C with respect to another object.

2.1.1 Energy Minimization and Speed Function Definition

Although the explicit and implicit active contour models differ both in their formulation and implementation, the common theme of all this work is the evolution of curves toward the boundary of an object through the solution of an energy minimization problem. In the following we provide some mathematical tools for deriving curve evolution equations from an energy functional $E(C)$. We are interested in finding an equation of motion for the curve that segments an image. Let us consider a variational approach for image segmentation formulated as finding the closed curve C such that

$$\tilde{C} = \min_C \{E(C)\} \quad (2.13)$$

In order to minimize $E(C)$ we evolve the curve iteratively over time t . The velocity field $\frac{\partial C}{\partial t}$ is often the best deformation δC that maximizes

$$\lim_{h \rightarrow 0} - \frac{E(C + h\delta C) - E(C)}{h} \quad (2.14)$$

In this sense, such a velocity field is called a gradient flow for the curve C . Computing a gradient flow for a general energy functional $E(C)$ is a not an easy task. As shown in Equation (2.15), the energy functional is usually composed of region integrals of the following form.

$$E(C) = \int_R F(x) dx \quad (2.15)$$

Given in the form of region integrals partial differential equations can be a solution to the problem of finding the best \tilde{C} in Equation (2.13). Since $F(C)$ denotes the first variation of $E(C)$, under general assumptions, the necessary condition for C to be the minimizer of $E(C)$ is $F(C) = 0$. The solution to this necessary condition can be computed as the steady state solution of the PDE

$$\frac{\partial C}{\partial t} = F \cdot \vec{N}. \quad (2.16)$$

The form of this equation indicates that F is the speed function for the evolution of C , and we are interested only in the part of F that points in the outward normal direction to the curve \vec{N} . To determine the appropriate speed function for segmentation application, underlies much of the research field in curve evolution theory. In chapter 3 and its sections we define how we construct our speed function or equivalently curve evolution equation in order to introduce coupled shape and inter-shape relative pose priors into the segmentation process.

2.1.2 Level Set Representation and Curve Evolution

The use of level set theory has provided more flexibility and convenience in the implementation of active contours. It was first introduced by Osher and Sethian in 1988. They are numerical techniques for tracking evolving surfaces, and they are properly used in a wide variety of applications. The level set methods can handle interfaces with sharp corners, cusps in any dimensional data in the presence of topological changes.

When using the level set evolution in image segmentation, we are seeking to detect the boundaries of some object or area in the image that we want to segment. This is done by initializing a curve or surface somewhere in the image, and then evolving it by letting appropriate forces act on it until it reaches the correct boundaries in the image. Level set methods use an implicit representation of the contour to represent the boundaries. Rather than describing the evolution of the contour itself, the level set approach operates on a function in one dimension higher and the interface is described as the isocontour of this function. In order to model an evolving contour, we let the level set function depend on time as well as space.

Let $\phi = \phi(x, t)$ be the level set function. Then the interface C , at a given point in time, t , is given as the set of points in space that corresponds to the zero level isocontour of ϕ , i.e. $C(t) = \{x : \phi(x, t) = 0\}$

The level set function $\phi : \Omega \times [0, \infty) \rightarrow \mathfrak{R}$ is a scalar valued function of both space and time variables. Since we restrict our attention to the image segmentation problem, ϕ is defined on the same rectangular domain as the image, $\Omega \subset \mathfrak{R}^n$. Usually we have $n = 2$ (a single 2D image) or $n = 3$ (an image volume, i.e. a set of image slices). The level set function is initialized at time zero and evolved in time until it stops. The function's time domain is $[0, \infty)$.

First an initial value for the level set function is built. This is done using the so-called signed distance function in which the initial value is constructed as

$$\phi_0 = \phi(x, t = 0) = \pm d. \quad (2.17)$$

Here $\pm d$ is the signed Euclidean distance from each point $x \in \Omega$ to the initial front assigning a positive distance if the point lies outside the region, and negative if inside the region. For points that lie on the initial interface, the distance is zero. Now the motion of the front is described by matching it with the zero isocontour of the level set function [53]. The level set value of a point on the front with path $x(t)$ is always zero as the interface evolves,

$$\phi(x(t), t) = 0. \quad (2.18)$$

Differentiating this equation with respect to time by the chain rule we obtain

$$\phi_t(x(t), t) + \nabla\phi(x(t), t) \cdot x'(t) = 0. \quad (2.19)$$

Here ϕ_t designates the partial derivative of ϕ with respect to t . Now, let F denote the speed that drives the evolution, more specifically, F is the speed in the outward normal direction to the level set interface. Then $F = x'(t) \cdot \vec{N}$ where \vec{N} is the outward unit normal to the level sets of ϕ , and $\vec{N} = \nabla\phi / |\nabla\phi|$. Manipulating Equation (2.19) we get

$$\begin{aligned} \phi_t + \frac{\nabla\phi}{|\nabla\phi|} \cdot x'(t) \cdot |\nabla\phi| &= 0 \\ \phi_t + (x'(t) \cdot \vec{N}) |\nabla\phi| &= 0 \end{aligned} \quad (2.20)$$

which brings us to the general form of the level set equation similar to equation (2.16)

$$\phi_t + F \cdot |\nabla\phi| = 0 \quad (2.21)$$

given $\phi(x, 0) = \phi_0$. If ϕ is a signed distance function, it satisfies the condition $|\nabla\phi| = 1$, [41]. In this case, the outward normal vector is given by

$$\vec{N} = \nabla\phi \quad (2.22)$$

which means that \vec{N} and $\nabla\phi$ point in the same direction with the assumption that velocity field F is defined only on the curve and the velocity outside the curve is assumed zero. In order to do that the value of the level set function ϕ is updated on the grid in the image domain. However we only increase the speed of the level set of the surface by a method called narrow band proposed by Chopp [54]. The goal of the speed function F is to act on the contour and pull it towards the edges of the image. Therefore, we model the speed function in such a way that when the contour reaches the desired position, the speed becomes zero.

After initializing ϕ at the grid points, the contour is moved across the grid by evolving ϕ forward in time by applying numerical methods to update its values. Let $\phi^n = \phi(t^n)$ represent the values of ϕ at a given point t^n in time. ϕ is updated by finding new values after some time increment Δt , i.e. finding $\phi^{n+1} = \phi(t^{n+1})$ where $t^{n+1} = t^n + \Delta t$. This is done using a simple first-order accurate method for the time discretization, the forward Euler method [41]. ϕ^{n+1} is computed by approximating ϕ_t at time t_n as

$$(\phi_t)^n = \frac{\phi^{n+1} - \phi^n}{\Delta t} \quad (2.23)$$

When this substituted into Equation (2.21), after rearranging terms, we get

$$\phi^{n+1} = \phi^n - \Delta t(F^n \cdot |\nabla \phi^n|). \quad (2.24)$$

where the superscripts in F^n and $|\nabla \phi^n|$ denote that the respective functions are evaluated at time t^n .

2.2 Nonparametric Density Estimation

Most statistical analysis tasks involve the use of probability density functions. For instance, Bayesian detection is based on the likelihood ratio, which is a ratio of two density functions. If we know the underlying densities, we can use them for the statistical analysis. In most cases we do not know these densities, so we estimate them. There are two types of estimation: parametric and non-parametric. Unlike the parametric density estimation where assumptions are made, the nonparametric density estimation makes less rigid assumptions about the distribution of the data. Nonparametric density estimation does not impose a structure on the density and learns the density function from data samples drawn from the unknown density. Considering a finite dimensional density estimate, Parzen density estimation is given by:

$$P(\tilde{x}) = \frac{1}{N} \sum_{i=1}^N k(x - X_i, \Sigma) \quad (2.25)$$

where X_1, X_2, \dots, X_N are samples drawn from a population with density function $f(x)$ and $k(x, \Sigma)$ is a m-dimensional gaussian kernel with covariance matrix Σ . If the kernel is spherical, i.e. $\Sigma = \sigma I$ the above density becomes

$$P(\tilde{x}) = \frac{1}{N} \sum_{i=1}^N k(d(x, x_i), \sigma) \quad (2.26)$$

where $d(x, x_i)$ is the Euclidean distance function and $k(x, \sigma)$ is a one dimensional Gaussian kernel.

Multivariate Parzen Density Estimation

In many applications we are not only interested in estimating the density of one random variable, but also density estimate of multiple random variables. Consider

an M -dimensional random vector $\mathbf{X} = (X_1, X_2 \dots X_M)$ where $X_1, X_2 \dots X_M$ are one dimensional random variables. Having N observations for each of the M random variables, the i^{th} observation of each of the M are collected in the vector \mathbf{X}_i .

$$\mathbf{X}_i = \{X_{i1} \dots X_{iM}\}, i = 1, 2, \dots, N \quad (2.27)$$

where X_{ij} is the i^{th} observation of the random variable X_j . Our goal is to estimate the joint pdf \mathbf{X} . From the previous experience with the one random variable case in the beginning of section 2.2, we might consider adapting the kernel density estimator to the M -dimensional case, and write:

$$f(\mathbf{x}) = \frac{1}{N} \sum_{i=1}^N k(\mathbf{x} - \mathbf{X}_i, \sigma_M) \quad (2.28)$$

$$= \frac{1}{N} \sum_{i=1}^N k((x_1 - X_{i1}, \dots, x_M - X_{iM}), \sigma_M) \quad (2.29)$$

Here k denotes a multivariate kernel function operating on M arguments. The solution for defining the form of the kernel k is to use a multiplication of separate kernels for M random variables. In this case Equation (2.29) becomes:

$$f(\mathbf{x}) = \frac{1}{N} \sum_{i=1}^N \prod_{j=1}^M k(d(x^j, x_i^j), \sigma_j) \quad (2.30)$$

2.3 Shape and Pose Analysis

When segmenting images of low quality or with missing data, the information obtained from images does not often provide enough contrast or clear boundary patterns of target objects. In such cases, prior information about the shape of the object can significantly aid the segmentation process. Therefore, the use of prior information based on shape and pose is gaining increased attention to segment images under such conditions.

As discussed in section 2.1, being a large research field, the problem is to extract such prior information from available example shapes and use it in segmentation. This section reviews some previous work in shape analysis and introduces shape priors into segmentation.

2.3.1 Shape Representation and Space of Shapes

There has been considerable amount of work in shape analysis and representation since the concept has been introduced by Kendall [55] and Small [56]. The first approach was to represent the object in image plane by finite number of salient points or landmarks. Regarding landmark based approach Cootes et al. [52] used principal component analysis (PCA) to reconstruct a typical shape and to compute shape variability from a training set of shapes. In this method the condition for good modeling is that training set should be as large as possible and the number of eigenvalues chosen in PCA should be appropriate according to the experiment. Furthermore, there is the issue of correspondence between landmarks among training shapes. The selection of landmarks was manual in the beginning which was not efficient and very complicated especially in 3D. Later in [57], [58] the authors proposed a way to select the landmarks automatically, yet this approach is computationally expensive.

Addressing the drawbacks of landmark based methods, there has been increasing interest in representing shapes via level set methods. As we mentioned in section 2.1, building shape priors from training shapes as signed distance functions and introducing into segmentation framework was initially proposed by [25]. In [25] and [45], PCA of the signed distance functions of training data is used to capture the variability in shapes. The statistical information that comes up with PCA, is used in segmenting noisy and occluded images. On the other hand the drawback of these methods is that the space of signed distance functions (SDF) is not closed under linear operations like addition or taking average. For example mean shape of a training set is not a reasonable SDF. As an effort to reduce this inconsistency Paragios et al. [21] estimated the mean shape by deforming shape in the direction of reducing its distance both from example shapes and from the space of SDFs. The main idea behind this approach is to perform a shape matching using the level set representations of the training examples. They construct a variational framework for the estimation of the best shape by seeking for the maximum likelihood of the shape density subject to the constraint of preserving SDF.

Another approach to represent a shape model is using maximum a posteriori (MAP) estimation framework in which a Bayesian formulation is constructed in

order to compute probability of shape given an image. In particular, in an active contour framework which involves level set methods, a nonparametric shape model is proposed based on the example shapes in a training set [32]. The underlying shape distribution is computed by extending a Parzen density estimator to the space of shapes. Now the question is how to compute such a probability measure on a set of shapes. Here the intuition is that a shape is more likely if it is similar to the shapes in the training set. The issue is to define a similarity measure which can be used in statistical analysis of shapes. Mathematically, this suggests defining distance metrics in the space of shapes to measure similarity and dissimilarity of shapes. The density estimation is done in infinite dimensional shape space which is a manifold embedded in Euclidean space. The authors extend the Parzen density estimate to an infinite dimensional one, following the Equation (2.26) in section (2.2). The unknown density of the shapes is computed as

$$P(C) = \frac{1}{N} \sum_{i=1}^N k(d_C(C, C_i), \sigma) \quad (2.31)$$

where d_C is a distance measure in infinite dimensional space C . Here the combination of one dimensional kernel and the distance metric together, behaves as an infinite dimensional kernel. For the kernel size σ , they use ML kernel size with leave one out [59]. In order to measure the similarity, they use metrics like L_2 and template metric for the space of shapes.

Geometric Properties Based on Moment Theory

In general, moments describe numeric quantities at some distance from a reference point or axis. Moments are commonly used in statistics to characterize the distribution of random variables, and, similarly, in mechanics to characterize bodies by their spatial distribution of mass. The use of moments for image analysis is straightforward if we consider a binary or grey level image segment as a two-dimensional density distribution function. In this way, moments may be used to characterize an image segment and extract properties that have analogies in statistics and mechanics. In this section we provide a short background on moments.

We take $f(x, y)$ as a binary map, where $f(x, y) = 1$ if (x, y) is inside an object,

and $f(x, y) = 0$ otherwise. Following [40], define the $(p + q)$ th order moment by

$$m_{p,q} = \int_{\Omega} x^p y^q f(x, y) dx dy$$

Definition of the discrete version of 2D moments

$$m_{p,q} = \sum_{x=0}^{N-1} \sum_{y=0}^{N-1} x^p y^q f(x, y),$$

Following [40], we mention that $m_{0,0}$ defines the area of the analyzed object. When computed for a silhouette image of a segmented object, the zeroth moment represents the total object area. Further, $\left\{ \frac{m_{1,0}}{m_{0,0}}, \frac{m_{0,1}}{m_{0,0}} \right\}$ provide the center of the mass of the analyzed object. These coordinates define a unique location with respect to the object that may be used as a reference point to describe the position of the object within the field of view. When the analyzed object is represented in a system of coordinates that has the origin in its center of mass, M_2 defines a canonic orientation of the analyzed object up to π radians. In addition, moments up to order two define a canonic orientation of the analyzed object up to π radians. The canonic axes senses (directions) are provided by M_3 , after canonic alignment (see [40]).

The second order moments $\{m_{2,0}, m_{0,2}, m_{1,1}\}$ known as the moments of inertia, may be used to determine the principal axes of the object. Besides, the angle developed by the canonic orientation of an object as related to a global reference coordinate can be computed as

$$\theta(C) = \frac{1}{2} \arctan \left(\frac{2(m_{1,0}m_{0,1} - m_{1,1}m_{0,0})}{(m_{0,2} - m_{2,0})m_{0,0} + m_{1,0}^2 - m_{0,1}^2} \right) \quad (2.32)$$

In section 3.2.2, we describe how we use moments for incorporating pose information about objects into segmentation process.

Chapter 3

Segmentation Based on Shape and Pose Priors

In this chapter we present our approach to the multi-object segmentation problem in detail. First, in section 3.1, we introduce the motivation of our work. In section 3.2, we introduce our general framework that we use for segmentation. In section 3.2.1 we describe our formulation for coupled shape prior. In section 3.2.2, we describe our formulation for inter-shape pose priors. In Section 3.3, we summarize the overall segmentation algorithm with implementation details.

3.1 Motivation for Coupled Shape and Inter Shape Pose Priors

Medical images are in general low quality images such that understanding some anatomical structures is a big challenge. In particular, segmentation of brain tissues, especially in the subcortical regions, remains a challenging task. This is mainly because of low intensity contrast in structural-MR images between the white matter (WM) and gray matter (GM) tissues in the subcortical regions that comprise structures such as the caudate, putamen, thalamus, etc. Considering that segmentation is equivalent to extracting the shape and the pose of the boundary of the object, prior information on both shape and pose would be helpful in segmentation, if we have any such information. In this context, statistical shape modeling and analysis is an important tool for understanding anatomical structures from medical images.

In many cases, objects to be segmented, have one or more neighboring structures, whose location and shape provide information about the local geometry that can aid in extracting the exact location. The analysis of the structures jointly, therefore, should introduce more information than studying them individually. In this fashion, the relative shape arrangements among these neighbors can be modeled based on statistical information from a training set. In the following section we introduce the interpretation of this model into active contour segmentation method in a nonparametric MAP estimation framework.

3.2 Segmentation Framework by Energy Minimization Based on Curve Evolution

In a typical active contour model, the segmentation process involves an iterative algorithm for minimization of an energy functional. We define our energy (cost) functional in a maximum a posteriori (MAP) estimation framework as

$$E(\mathbf{C}) = -\log P(\text{data}|\mathbf{C}) - \log P(\mathbf{C}), \quad (3.1)$$

where \mathbf{C} is a set of evolving curves $\{C^1, \dots, C^m\}$ that match the boundary of m different shapes. We choose the likelihood term $P(\text{data}|\mathbf{C})$ as in [18], and refer to the corresponding force as C&V which are the initials of the author's names. $P(\mathbf{C})$ is a joint prior density of multiple objects. In this work we focus on building $P(\mathbf{C})$.

The joint prior is evaluated using a training set of N shapes of the objects $\{\mathbf{C}_1, \dots, \mathbf{C}_N\}$. The essential idea of using such a prior is that a candidate segmenting curve \mathbf{C} will be more likely if it is similar to the example shapes in the training set. So we compare the candidate curves with training examples. In order to provide direct comparison, the candidate curve \mathbf{C} and the training examples $\{\mathbf{C}_1, \dots, \mathbf{C}_N\}$ should be aligned since shape distances are not invariant under translation, rotation and scale. Therefore, the pose variation of one object in the training set is removed where we still keep the relative pose variations of objects among each other. We do the alignment operation, as in [45] where a set of similarity transformation parameters (translation, scaling and rotation) are calculated for each sample in the training set to align binary shapes with each other. During this operation $\{\mathbf{C}_1, \dots, \mathbf{C}_N\}$ are

aligned into $\{\tilde{\mathbf{C}}_1, \dots, \tilde{\mathbf{C}}_N\}$.

In the segmentation framework, to build joint prior according to the training set we relate each candidate segmenting curve \mathbf{C} with its aligned version $\tilde{\mathbf{C}}$ such that $\tilde{\mathbf{C}} = T[\mathbf{p}]\mathbf{C}$. All evolving contours are aligned relative to the training set via similarity transformation $T[\mathbf{p}]$ where \mathbf{p} is a vector of pose parameters (p_1, \dots, p_m) for each object. Each p_i , $(i = 1, 2, \dots, m)$ corresponds to a vector of translation, rotation and scale parameters that are updated at each iteration during the evolution. In this context, we define the joint prior $P(\mathbf{C})$ in terms of the pose and shape parameters of multiple objects such that

$$P(\mathbf{C}) = P(T^{-1}[\mathbf{p}]\tilde{\mathbf{C}}) = P(\tilde{\mathbf{C}}, \mathbf{p}) \quad (3.2)$$

We differentiate between the shape and pose prior information:

$$P(\tilde{\mathbf{C}}, \mathbf{p}) = P(\tilde{\mathbf{C}}) \cdot P(\mathbf{p}|\tilde{\mathbf{C}}) \quad (3.3)$$

Now, the problem is to define the coupled shape prior $P(\tilde{\mathbf{C}})$ and the joint pose prior $P(\mathbf{p}|\tilde{\mathbf{C}})$ of the multiple objects.

We compute the coupled shape density where we avoid all the pose artifacts and consider only shape variability. We describe its formulation in section 3.2.1. We compute the joint pose prior in order to model the variability of relative positions of objects. In a previous work [60], $P(p|\tilde{\mathbf{C}})$ was assumed to be uniform with the assumption that all poses \mathbf{p} are independent and equally likely. In that specific case, $P(\mathbf{C})$ could be computed directly as:

$$P(\mathbf{C}) = P(\tilde{\mathbf{C}}) \cdot \gamma. \quad (3.4)$$

where γ is a normalizing constant. If the prior information about the pose $P(p|\tilde{\mathbf{C}})$ is available, one can use that information. For example, in a more general case, the positions of each object might be dependent and the joint distribution of $P(p|\tilde{\mathbf{C}})$ can be defined among globally aligned training examples. In this approach the main idea is that the position of each object is defined by a global and internal pose parameters. We call the position of the object set as a whole, where position parameters (translation, rotation and scaling) are computed for all objects at once, a global position. Beyond global position, we define internal positions of individual

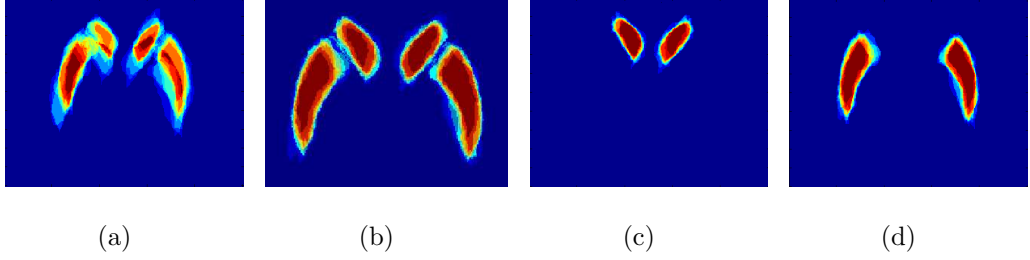


Figure 3.1: Alignment of training shapes for Nucleus Caudate (NC) and Putamen (P). (a) superposition of unaligned binary shapes of multiple objects (NC + P), (b) superposition of globally aligned binary shapes of multiple objects (NC + P) (c) superposition of locally aligned binary NC shapes, (d) superposition of locally aligned binary P shapes

objects as local pose differences among the multi-object set. In this context, \mathbf{p} is composed of

$$\mathbf{p} = (p_{glb}, p_{int}^1, \dots, p_{int}^m) \quad (3.5)$$

parameters. Using definition in Eq. 3.5 we reinterpret the Eq. 3.3 as:

$$P(\tilde{\mathbf{C}}, p) = P(\tilde{\mathbf{C}}) \cdot P(p_{glb}, p_{int}^1, \dots, p_{int}^m | \tilde{\mathbf{C}}) \quad (3.6)$$

Here we propose that p_{glb} and $\mathbf{p}_{int} = (p_{int}^1, \dots, p_{int}^m)$ are independent parameters. Since p_{glb} and \mathbf{p}_{int} are independent, we have

$$P(\tilde{\mathbf{C}}, p) = P(\tilde{\mathbf{C}}) \cdot P(p_{glb} | \tilde{\mathbf{C}}) \cdot P(\mathbf{p}_{int} | \tilde{\mathbf{C}}) \quad (3.7)$$

Here, $P(p_{glb} | \tilde{\mathbf{C}})$ is assumed to be uniform. Following Eq. 3.4 we can define $P(\mathbf{C})$ as

$$P(\mathbf{C}) = P(\tilde{\mathbf{C}}) \cdot \gamma \cdot P(\mathbf{p}_{int} | \tilde{\mathbf{C}}) \quad (3.8)$$

Substituting $P(\mathbf{C})$ into Equation (3.1), we obtain

$$E(\mathbf{C}) = -\log P(data | \mathbf{C}) - \log P(\tilde{\mathbf{C}}) - \log P(\mathbf{p}_{int} | \tilde{\mathbf{C}}) \quad (3.9)$$

Given Eq. 3.9, the focus of our work is to define the priors $P(\mathbf{p}_{int} | \tilde{\mathbf{C}})$ and $P(\tilde{\mathbf{C}})$. During the segmentation, following Eq. 3.2 we relate evolving candidate curves \mathbf{C} to aligned curves $\tilde{\mathbf{C}}$ via transformation $T[\mathbf{p}]$ such that $P(\mathbf{C}) = P(T^{-1}[\mathbf{p}] \tilde{\mathbf{C}})$ as presented before in [32] which focuses single object segmentation. Beyond [32], we relate the

evolving curves to aligned curves according to both global and internal pose parameters. During the alignment which is a preprocessing step in the training, we first align multi-object samples globally and then align individuals locally. One can see the difference between global and local alignment of training examples for two Basal Ganglia structures in Figure 3.1. Figure 3.1 (a) shows superposition of unaligned multi-object samples. Figure 3.1 (b) shows the superposition after global alignment. Figure 3.1 (c) and (d) show superposition after local alignment for separate structures. Comparing (b) with (c) and (d) one can observe the scale factor and sharpness in the superimposed images. For the sake of simplicity of exposition, and without loss of generality, we present inter-shape pose issues between two objects only. However, the framework we develop is general enough to be applied to arbitrary number of objects.

3.2.1 Coupled Shape Prior for Multiple Objects

In this section, we construct the coupled nonparametric shape prior information $P(\tilde{\mathbf{C}})$ for m different classes of objects. To build a joint prior model for multiple objects, we choose level sets as the representation of shapes [41] and we use multivariate Parzen density estimation (see [61]) to estimate the unknown joint shape distribution. Consider $m = 2$ (CN and P only) and define the joint kernel density estimate of two shapes as,

$$P(\tilde{C}^1, \tilde{C}^2) = \frac{1}{N} \sum_{i=1}^N \prod_{j=1}^{m=2} k(d(\phi_{\tilde{C}^i_j}, \phi_{\tilde{C}^j_i}), \sigma_j) \quad (3.10)$$

where $k(\cdot, \sigma_j)$ is a Gaussian kernel with standard deviation σ_j . In this equation, $\phi_{\tilde{C}^i_j}$ is the candidate SDF of j^{th} object, aligned to the training set and $\phi_{\tilde{C}^j_i}$ is the SDF for the i^{th} training shape of the j^{th} object. Note that, given a distance measure $d(\cdot, \cdot)$, we can construct the kernel for joint density estimation, by multiplying separate kernels $k(\cdot, \sigma_j)$ for each object. Our nonparametric shape prior in (3.10) can be used with a variety of distance metrics. In this work, we consider the L_2 distance d_{L_2} between SDFs as in [32]. For the kernel size σ_j , for the j^{th} object, we use maximum likelihood kernel size with leave-one-out method (see [59]).

Our joint shape density involves modeling of inter-relationships among multiple shapes, a capability that was not proposed in the current state of the art single

shape prior based approaches (see, for example, [25], [32]). As compared to existing single shape prior based approaches in this framework, we produce much more accurate joint shape densities in cases where there are shape dependencies between the multiple objects involved. This is a phenomenon we observe in basal ganglia structures.

Gradient Flow for the Coupled Shape Prior

In this part, we compute a gradient flow for the joint prior in equation (3.10) for the two curves which are represented implicitly by their corresponding SDFs.

In differentiating the logarithm of the expression given in (3.10), we use shorthand notation, k_{σ_j} for $k(d_{L_2}(\phi_{\tilde{C}_j}, \phi_{\tilde{C}_i}), \sigma_j)$. Note that $\phi_{\tilde{C}_i}$ is a function of iteration time t and $\phi_{\tilde{C}_j}$ is a shorthand notation for the evolving level set function $\phi_{\tilde{C}_j}(t)$. Using these conventions, we obtain

$$\frac{\partial}{\partial t} \log P(\tilde{C}^1, \tilde{C}^2) = \frac{1}{N} \frac{\sum_{i=1}^N \{k'_{\sigma_1} k_{\sigma_2} + k_{\sigma_1} k'_{\sigma_2}\}}{P(\tilde{C}^1, \tilde{C}^2)} \quad (3.11)$$

Then, we compute the gradient flow in the normal direction that increases most rapidly for each object curve. Using the L_2 distance in kernels, we find that the gradient directions for the curves \tilde{C}^j are (see Appendix A):

$$\frac{\partial \phi_{\tilde{C}^j}}{\partial t} = \frac{1}{\sigma_j^2} \sum_{i=1}^N \lambda_i(\tilde{C}^1, \tilde{C}^2) (\phi_{\tilde{C}_i^j}(x, y) - \phi_{\tilde{C}^j}(x, y)) \quad (3.12)$$

where $j = 1, 2$, $\lambda_i(\tilde{C}^1, \tilde{C}^2) = \frac{k(d_{L_2}(\phi_{\tilde{C}_i^1}, \phi_{\tilde{C}_i^1}), \sigma_1) k(d_{L_2}(\phi_{\tilde{C}_i^2}, \phi_{\tilde{C}_i^2}), \sigma_2)}{N \cdot P(\tilde{C}^1, \tilde{C}^2)}$, and $\sum_{i=1}^N \lambda_i(\tilde{C}^1, \tilde{C}^2) = 1$. The final expression (3.12), evolves the curves toward shapes at the local maximum of the coupled shape prior of two objects. Note that, training shapes that are closer to the evolving curve get more weight. Furthermore, the weighting function λ_i depends on each curve in exactly the same way. In particular, due to the coupled nature of this weight, given a pair $(\tilde{C}_1, \tilde{C}_2)$ in the evolution process training shape pairs in which the second training shape is closer to \tilde{C}_2 get relatively more weight in the evolution of the *first* curve as well. This shows one aspect of the coupled nature of our shape-based segmentation approach.

3.2.2 Moment-based Relative Pose Prior for Multiple Objects

In a multiple object system, the pose of the objects as related to their gravity center is computed via moments. Define p_{int}^j as the set of internal pose parameters, where C^j is a curve defining object j . We define $p_{int}^j = \left[m_{0,0}, \frac{m_{1,0}}{m_{0,0}}, \frac{m_{0,1}}{m_{0,0}}, \Theta \right]$ as a vector of real values which correspond to scale, translations and rotation respectively. They are computed from level set representation of each curve via standard moments (see Appendix B for details). We estimate $P(\mathbf{p}_{int} | \tilde{\mathbf{C}})$ using Parzen kernel density estimation in a similar way to Section 3.2.1 as follows

$$P(\mathbf{p}_{int} | \tilde{\mathbf{C}}) = \frac{1}{N} \sum_{i=1}^N \prod_{j=1}^2 k(d(p_{int}^j, p_{int}^{j_i}), \sigma_j), \quad (3.13)$$

where k is a Gaussian kernel. We define a Mahalonobis distance between the pose parameters of the candidate curve and the training curves being the second weighted norm of the difference vector. $d(p_{int}^j, p_{int}^{j_i}) = \|p_{int}^j - p_{int}^{j_i}\|_2$. Note that computing the norm of the difference vector, we consider weighting coefficients for each term of p_{int}^j . We compute the coefficients by normalizing into $[0, 1]$ in order to compute normalized values which are reasonable norms for each type of pose parameter.

Gradient Flow for the Relative-Pose Prior

In this part, we define a gradient flow for the joint pose prior in Eq. (3.13) in order to minimize the cost functional in Eq. (3.9). We use one curve for each object and they are represented implicitly by their corresponding SDFs. During the evolution of the level sets, the inter-shape pose parameters p_{int}^j are updated. During this update, to minimize the cost functional in Eq. (3.9), instead of computing the gradient descent for each explicit pose parameter, we compute the update for the signed distance functions (SDF) of the objects \tilde{C}^j at each iteration time step since the pose parameters are represented in terms of moment values computed over SDFs. This key point shows the merit of using moments, then we can introduce pose priors in order to make local deformations in the evolving curves.

Following Eq. (3.13), we obtain the update for pose based evolution as

$$\frac{\partial \Phi_{\tilde{C}^j}}{\partial t} = \frac{1}{P(\mathbf{p}_{int} | \tilde{\mathbf{C}}) \cdot N} \sum_{i=1}^N \frac{k_{\sigma_1} k_{\sigma_2}}{-\sigma_j^2} MPF(j, i), \quad (3.14)$$

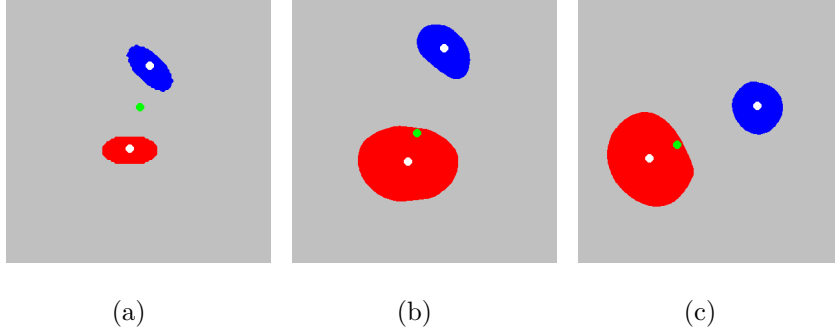


Figure 3.2: Moments based inter-shape pose reconstruction. The small white circles are the mass centers of the corresponding objects. The green small circles are the mass centers of the blue and red objects together. (a) initialization, (b) iteration 140, (c) steady state after iteration 200.

where

$$\begin{aligned}
MPF(j, i) &= (\tilde{m}_{0,0} - \tilde{m}_{0,0}^i) \\
&+ \sum_{(r,s) \in \{(1,0), (0,1)\}} \left(\frac{\tilde{m}_{r,s}}{\tilde{m}_{0,0}} - \frac{\tilde{m}_{r,s}^i}{\tilde{m}_{0,0}^i} \right) \frac{(x^r y^s \tilde{m}_{0,0} - \tilde{m}_{r,s})}{\tilde{m}_{0,0}^2} \\
&+ (\tilde{\theta} - \tilde{\theta}^i) \sum_{r=0}^2 \sum_{s=0}^{2-r} x^r y^s M_{r,s}^\theta
\end{aligned} \tag{3.15}$$

for each $j \in \{CN, P\}$. Here, $\tilde{m}_{r,s}$ denotes moments of aligned evolving curve, $\tilde{m}_{r,s}^i$ means moments of the aligned training i th image, whereas the rotation angles θ follow similar conventions. Note that, the moments and the rotations depend on j . In the equation, the short notation term $M_{r,s}^\theta$ depends on θ (of the evolving CN or P). Its complete definition and all elaborations are part of Appendix.

We provide an example for the inter-shape pose prior based curve evolution in Figure 3.2. To construct prior distribution, in the training set, we use only one training sample in which we have two arbitrarily positioned parallel ellipses with size ratio of 3 and the same θ angles with the principal axis of the whole system. Looking at the table 3.1, one can understand that the ratio of distances between centers of the objects and mass center is also 3 since their size ratio is 3. In the figure each white small circle shows the mass center of the corresponding ellipse. The small green circle is the mass center of both ellipses. We illustrate the moment based evolution towards the reconstruction of the inter-shape pose of two ellipses in Figures 3.2 (a), (b), and (c). In (a) arbitrary initialization with same sizes is shown.

	Blue Object		Red Object	
	Area	MCD	Area	MCD
Training	471	45	1413	15
Initialization	153	17.91	299	9.16
Iteration 140	482	43.71	1471	14.32
Steady state	503	41.1	1465	14.15

Table 3.1: Area and mass center distance (MCD) reconstruction measurements in pixels. MCD is the distance between the white (corresponding) mass center and the green one in pixels.

In (b) one can see the result after a certain amount of iteration where the size ratio of two ellipses and the distance between center of masses are reconstructed according to training sample. Note that the relative orientation of the ellipses is also recovered, as shown in Figure 3.2 (c). In this experiment, considering only relative position information we converge to a local minima in order to obtain corresponding ratios for the objects in the training sample where we disregard global position information. The area measurements and mass centers positions of the blue and red objects are shown in Table 3.1.

3.3 Segmentation Algorithm

In this section we summarize the segmentation algorithm with implementation details. We describe our algorithm in Figure 3.3. In an iterative segmentation process, we show the basic utilities that provides data force, shape force and pose force in separate branches of the diagram. We start the procedure with the initializations of the segmenting curves correspond to separate structures. This initialization can be simple curve / sphere pair put inside the target structures. Having initial curves, we generate SDFs and, as shown in the top branch, for a certain amount of iterations we drive the curves using only data force (C&V) without any training information. After a certain stage, at each iteration, we continue to update the SDFs ϕ by adding the C&V, the coupled shape, and the inter-shape pose forces (2^{nd} and 3^{rd} branches) together, until the curves reach steady state. We use a local optimization scheme

(in particular, gradient descent) to find a local minimum of our non-convex cost functional.

During iterations we relate segmenting curves to the training set samples via transformation $T[\mathbf{p}]$ to compute coupled shape and inter-shape pose priors. In order to do that, describing each candidate curve by its shape and pose, we interpret $\tilde{\mathbf{C}}$ as the shape of \mathbf{C} after being transformed by $T[\mathbf{p}]$. Before adding forces together we retransform the curves into test image domain by $T^{-1}[\mathbf{p}]$. Regarding sensitivity to transformation issues, we wait for the curves to reach to a reasonable shape before computing prior forces, since shape distances are not invariant under translation, scale and rotation. For details, see Eq. (3.12) and (3.14) respectively.

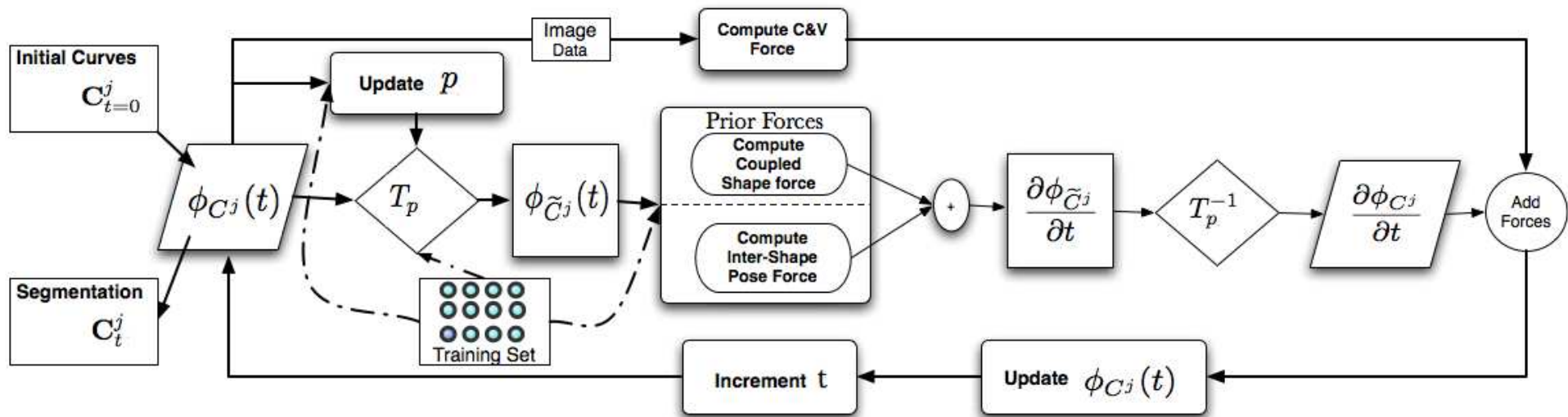


Figure 3.3: Segmentation Algorithm - In each step, three forces are evaluated: C&V, Coupled Shape (see Section 3.2.1), and Inter-Shape Pose (see Section 3.2.2)

Chapter 4

Experimental Results

Now we present experimental results demonstrating our segmentation method based on nonparametric coupled shape and inter-shape pose priors of multiple objects. We show several segmentation results for the head of Caudate Nucleus and the Putamen of brain Basal Ganglia. Here the coupled shape prior not only involves the shape prior of separate objects but also captures the coupled shape information of multiple objects. Inter-shape pose prior involves parameters such as the distance between objects, surface area and relative orientation of individuals among each other. In our experiments, we demonstrate the effects of coupled shape and inter-shape pose prior in comparison with the C&V force (see [18]) and the single shape prior (see [32]) based segmentations. During the experiments, we differentiate between the results on synthetic and real MR images. We perform a quantitative analysis of the accuracy of the segmentations in terms of false positive (FPR) and false negative (FNR) rates, (see [62]), as well as Dice coefficients DC (see [63]). Our ground truths are binary images which were created by a medical operator who manually segmented the Caudate Nucleus and the Putamen of real brain MR images. A user guided interface was used for this task. Figure 4.1 shows a picture of the interface that is used by an operator to segment structures that we focused in the experiments. Our synthetic data is created on top of the ground truth shapes by adding noise. As for real images, we present results on proton density (PD) and T2 MR images, which present challenges due to their low contrast. In all the result images, the blue, red, and green small circles, represent the mass centers of the Caudate Nucleus, the Putamen, and the joint mass center, respectively. One hundred iterations require twenty five seconds for computing the coupled shape forces and eighty seconds for

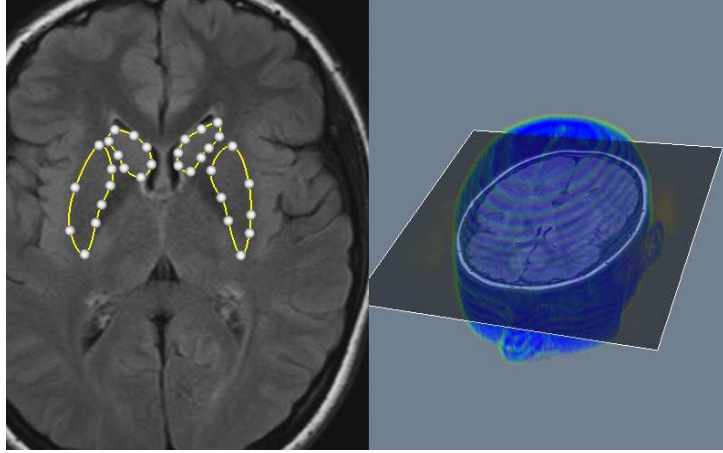


Figure 4.1: A picture of interface that is used for manual segmentation.

computing inter-shape pose force, in average. We use 512x448 pixels images and run the proposed segmentation scheme on a Core 2 Duo Pentium with 3GHz speed. Based on the condition of the initial curve or surface, it takes between 100 and 200 iterations to converge to a steady state situation. If the initial curves are far from the target structure it requires more time to obtain a good segmentation.

4.1 Synthetic Data

In this section, we demonstrate our coupled shape and relative pose prior based segmentation algorithm with the segmentation of synthetic brain structure images. We use twelve ground truths of the Caudate Nucleus and Putamen extracted manually as shown in Fig. 4.1. We choose one binary ground truth and add noise to it towards segmentation testing, whereas the rest of the ground truths are used in training. We work with high contrasted Caudate Nucleus and low contrasted occluded Putamen, in order to show the effect of using the coupled shape and inter-shape pose priors. The results of one round are shown in Fig. 4.2. The C&V method (see Fig. 4.2 (a)) cannot recover the occluded part of Putamen. The result of using single shape prior of separate objects provides better segmentation for the occluded part (see 4.2 (b)). In particular, Fig. 4.2(c) shows the effect of using relative pose prior of two objects. Here we intend to show the merit of using moment based relative pose prior such that it improves the result although it is used without shape prior (com-

Prior	P		
	FPR	FNR	1-DC
Single Shape	0.024	0.091	0.177
Pose	0.012	0.183	0.195
Shape & Pose	0.004	0.06	0.07

Table 4.1: Average quantitative accuracy results for the experiment shown in figure 4.2

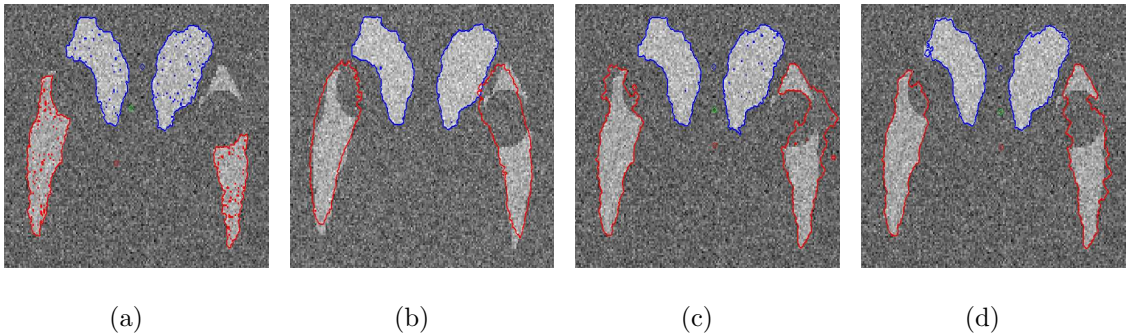


Figure 4.2: Segmentations on synthetic data. (a) C&V method, (b) single shape [32], (c) inter-shape pose only, (d) proposed coupled shape and inter-shape pose priors.

pare 4.2(a) and 4.2(c)). Using coupled shape and inter-shape pose prior together provides better segmentation than the other results in Fig. 4.2, as seen in (d). The coupled shape and inter-shape pose forces try to push or expand the contour to cover the bottom parts of the Putamen. They try to shrink the upper parts and also recovers the occluded regions of Putamen. Regarding the qualitative results shown in Fig. 4.2 we illustrate the average validation results of Putamen in twelve leave one out experiments (see Table 4.1). All three performance criteria indicate superior accuracy when using coupled shape and inter-shape pose priors together.

4.2 Real Data

In this section we demonstrate the results of segmentation for proton density and T2 MR data. We first show the results using only coupled shape prior. In the next group of experiment we show several segmentation results using not only coupled shape prior but also adding inter-shape pose prior of multiple objects. We demonstrate the effects of coupled shape and inter-shape pose prior in comparison with the C&V force ([18]) and the single shape prior ([32]) based segmentations.

In the first experiment on real MR data, we apply our coupled shape prior based segmentation method to segment the head of Caudate Nucleus and Putamen. We use a training set of twenty binary shapes that include the focused structures. We compare our multi object coupled prior with single object prior. The benefit of using a coupled prior is expected to be greater when the boundary of some objects is not well supported by the observed image intensity. We demonstrate the results for several images in Fig. 4.3. The first column in Fig. 4.3 show the results of using only intensity based curve evolution method [18] using only curve length penalty as the regularizing term in the energy functional. This method presents serious leakages for both structures. Figure 4.3 second and third columns show the single shape prior based results for separate structures. Both of the structures can not be effectively extracted because the samples in the training set for separate structures cause the corresponding curves to collapse into them. Here, the training set includes structures taken from sequential slices of several patients. The variability in their geometry and shape is very high. In fact this is a problem in clinical applications, too. Depending on the spacing between slices, the shapes of the structures that stays in adjacent slice levels varies significantly. During the evolution of related contour, the highest weighted train sample corresponds to one which is extracted from a different slice level. According to the results for Putamen, this method presents a considerable amount of miss in Putamen. The contour can not catch all the regions belongs to Putamen. For the head of Caudate Nucleus it also presents miss and small leakages towards the Ventricles. With the proposed coupled shape prior (force), both structures can be segmented more effectively due to the fact that coupling effect between shapes provides higher weighting for the train samples extracted from the proper slice levels (see Fig. 4.3 last column). Average segmentation error rates

Prior	CN			P
	FPR	FNR	1-DC	1-DC
Single shape	0.0165	0.071	0.19	0.15
Coupled shape	0.0098	0.044	0.11	0.10

Table 4.2: Average quantitative accuracy results for the experiments in figure 4.3

Prior	CN			P
	FPR	FNR	1-DC	1-DC
Single shape	0.005	0.112	0.18	0.04
Pose	0.0039	0.132	0.151	0.108
Shape & Pose	0.003	0.065	0.1	0.08

Table 4.3: Quantitative accuracy results for the experiments in figure 4.2.

given in Table 4.2 qualitatively confirm the superior performance attained using our coupled prior.

In the second experiment on real MR data, we apply our coupled shape prior based segmentation method to segment only left part of Caudate Nucleus and Putamen. We use a training set of twelve binary shapes that include only the left part of the focused structures. The C&V method results in inevitable leakages for both NC and P (see Figure 4.2 (a)). The result of the method that uses single shape prior is shown in Figure 4.2 (b) for each structures. The result of the moment based inter-shape pose prior is shown in Figure 4.2 (c). The inter-shape pose prior alone bounds leakages. One can understand that the moment based curve evolution provides significant amount of reduction in leakages as compared with the method in (a). It brings area, distance and rotation constraints into segmentation naturally. Besides, the synergy of the coupled shape and the inter-shape pose priors provides the best overall performance (consider structures together), as shown in Figure 4.2

	CN	P
Prior	1-DC	1-DC
C&V Force	0.42	0.39
Single Shape	0.123	0.179
Coupled Shape	0.112	0.131
Shape and Pose	0.109	0.121

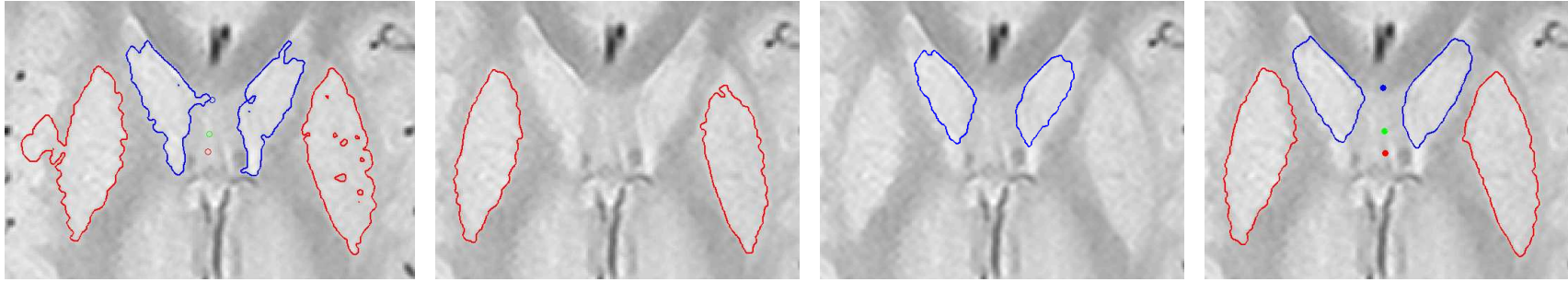
Table 4.4: Average quantitative accuracy results for the experiments in figure 4.5

(d). We show the achieved accuracy by means of three error rate parameters in Table 4.2.

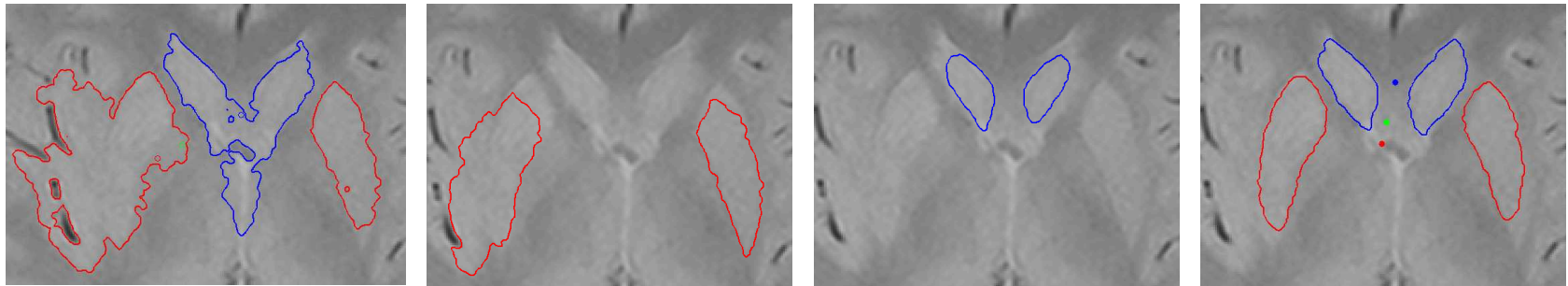
In another experiment, we compare the segmentations of the complete head of Nucleus Caudate and Putamen by using three methods. We demonstrate the results of this experiment in Figure 4.5. During the experiments for three different method, we start with the same initial conditions and show the results obtained in steady state. We use the same data term (C&V) in each method. The usage of same data term simplifies the comparison of our approach among others since only the coupled shape or inter-shape pose prior components of the methods are different. The C&V method, alone, results in inevitable leakages for both Nucleus Caudate and Putamen (see Figure 4.5 first column). In the second and third column, we show the results obtained by using single shape prior for separate structures. This method performs well for the Putamen in first and second rows. On the other hand it presents misses in the Nucleus Caudate for the same images. The result of the proposed coupled shape prior using globally aligned structures (without using pose prior) is shown in Figure 4.5 (forth column). One can see that the coupled shape force recovers the misses of the Nucleus Caudate and provides almost same performance for the Putamen. When applying the synergy between the coupled shape and the inter-shape pose forces we reduce the error in Putamen and Nucleus Caudate for all images. This result is shown in Figure 4.5 (fifth column). We also show the achieved average accuracy by means of the DC parameters in Table 4.4.

Next experiment is on 3 dimensional data. We present surface evolution for Nucleus Caudate and Putamen in Figure 4.6. Blue volume corresponds to ground truth of the Nucleus Caudate and green volume corresponds to the ground truth

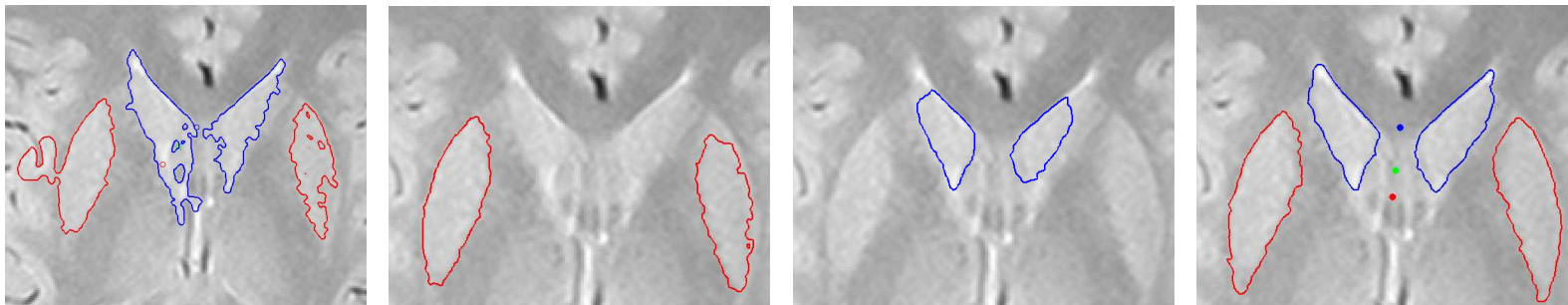
of Putamen. We show segmenting active surface in red and violet for NC and P, respectively in Figure 4.6 (a). We show the axial section of the brain in gray scale intensity with the plane Z. We show the results with using only data based force (C&V) in Figure 4.6 (b). We show coupled shape prior based evolution result for both structures in Figure 4.6 (c). According to (c), the volumetric targets can be captured accurately by the evolving surfaces of the both structures.



(e) Experiment on PD MRI data



(j) Experiment on T2 MRI data



(o) Experiment on PD MRI data

Figure 4.3: Segmentation results of the CN and the P in an MR slice: (First column) C&V method, (Second column) single shape prior only (Putamen), (Third column) single shape prior only (head of Caudate), (Forth Column) proposed coupled shape prior.

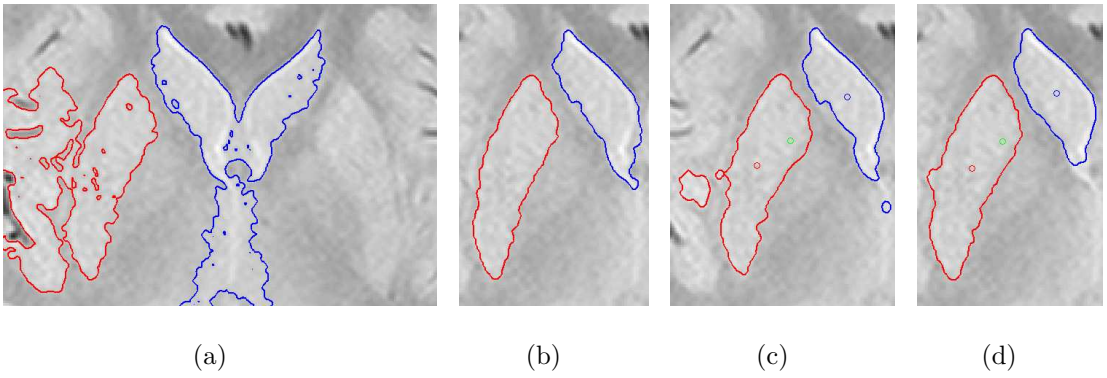
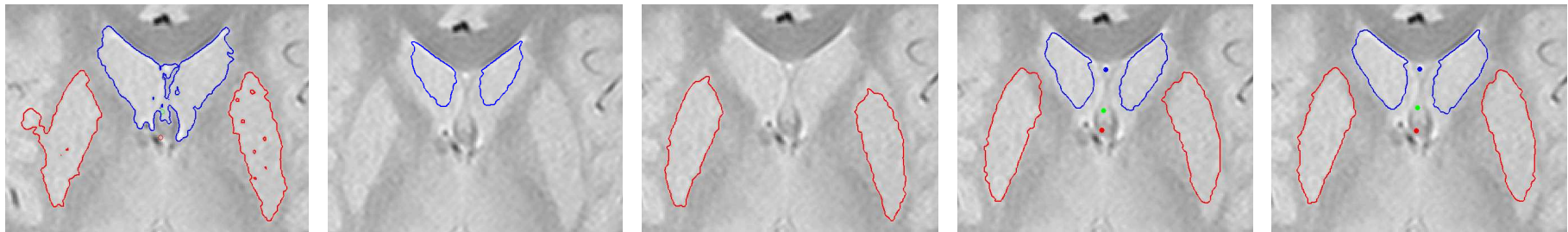


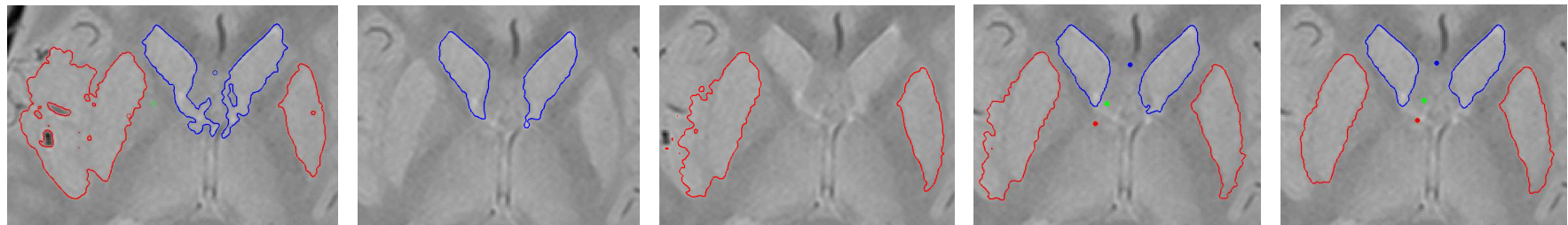
Figure 4.4: Segmentation results of the left part of the CN and the P in an MR slice: (a) C&V method, (b) single shape prior only (see [32]), c) inter-shape pose prior only, (d) proposed coupled shape and inter-shape pose prior.



(f) Experiment on PD MRI data



(l) Experiment on PD MRI data



(r) Experiment on T2 MRI data

Figure 4.5: Segmentation results of the CN and the P in an MR slice: (First column) C&V method (see [18]), (Second and Third column) single shape prior, (Forth column) proposed coupled shape prior only, (Fifth column) proposed coupled shape and inter-shape pose prior.

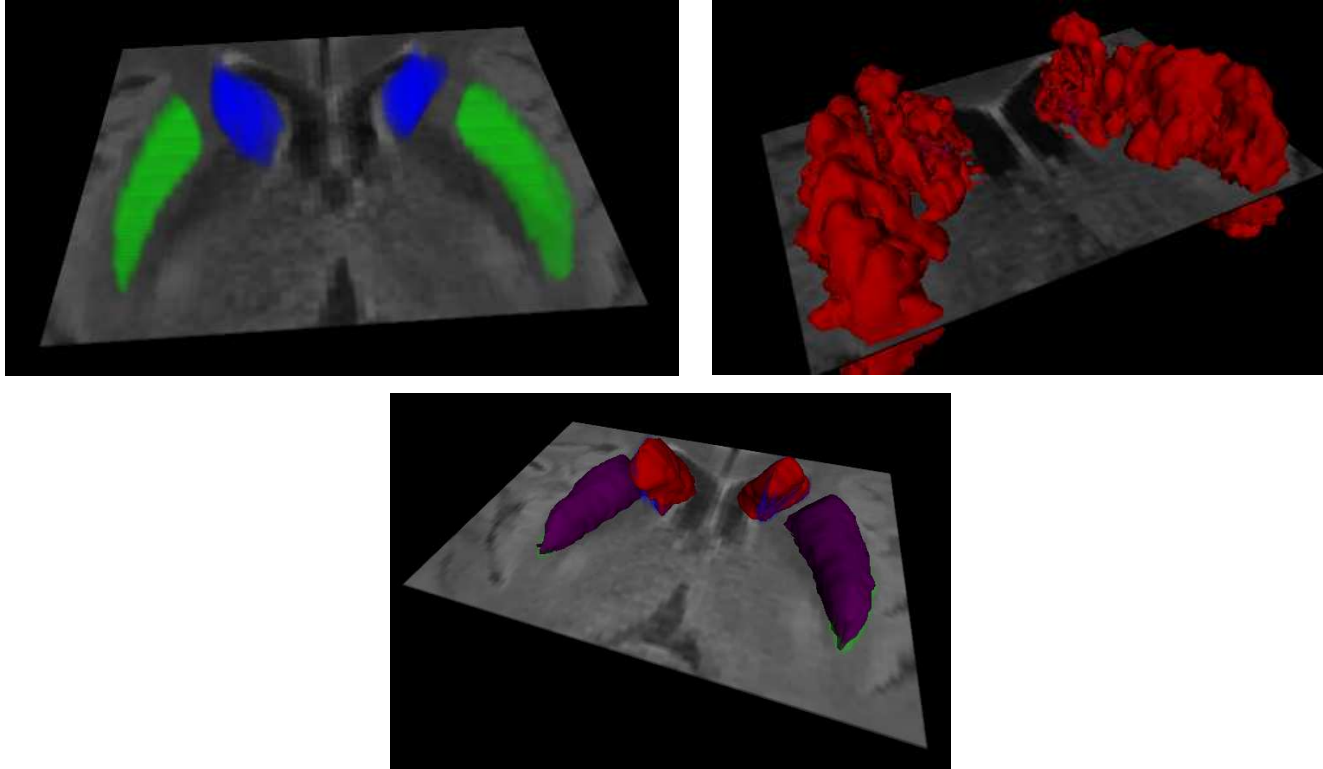


Figure 4.6: 3D segmentation: (a) Volumetric representation of target structures, segmentation results of the CN and the P in an MR volume (b) Using only ChanVese, (c) Using coupled shape prior

Chapter 5

Conclusion

5.1 Summary

Brain tissue segmentation in MR images is a fundamental problem in clinical studies of brain structure and function. Efficient computer-assisted segmentation of internal anatomy that produce accurate results is limited since many important structures in MR images do not present a clear boundary for segmentation and have variations between different subjects. In particular, segmentation of brain tissues, especially in the subcortical regions, remains a challenging task. This is mainly because of low intensity contrast in structural-MR images between the white matter (WM) and gray matter (GM) tissues in the subcortical regions that comprise structures such as the caudate, putamen, thalamus, etc.

Considering that segmentation is equivalent to extracting the shape and the pose of the boundary of the object, prior information on both shape and pose would be helpful in segmentation, if we have any such information. In this context, statistical shape modeling and analysis is an important tool for understanding anatomical structures from medical images. In many cases, objects to be segmented, have one or more neighboring structures, whose location and shape provide information about the local geometry that can aid in extracting the exact location. In this thesis, we have proposed a multi-object segmentation approach that employs coupled shape and inter-shape pose prior information of different Basal Ganglia structures. In an active contour framework, we achieve multi-object segmentation by evolving different curves in parallel. We use the training information of structures that we are interested, to estimate the coupled shape information as well as the inter-relationship

pose information among them. For coupled shape priors, we propose nonparametric density estimates based on signed distance functions (SDF) of training shapes. For inter-shape pose priors, we use standard moments, which are intrinsic to shape and have natural physical interpretations. We compute the probability density of joint pose prior based on SDFs, too. We apply pose effect on evolving contours as local deformations in order to obtain more accurate segmentation. We have demonstrated our approach in several experiments, with comparisons to other techniques to show the superiority of our coupled shape and joint pose priors.

5.2 Future Work

In the following we provide several topics for future research. We suggest several ways to increase the accuracy of the segmentation results. Our nonparametric priors were used on top of a weak data based likelihood term where we wanted to show the merit of our approach. However for more specific purpose cases, introducing a more structured data term, based on intensity characteristics or texture properties of the tissues could be considered. Initializations based on atlas based registrations could provide faster and better results since our framework is based on gradient descent optimization.

Our inter-shape interaction is based on relative pose information among multiple objects. More complex inter-shape interactions can be used to introduce into segmentation other than just pose. Also other multi object shape modeling approaches can be used with our moment based pose interaction.

Another future work topic would be that, in medical imaging there are many imaging modalities, each of them provide different facilities for specific purposes. Multi modality processing can be used to provide better data fidelity in order to increase segmentation accuracy in the presence of low contrast or inhomogeneity.

The results of our segmentation can be also used for shape analysis to examine relationships between structural abnormalities and deformations and certain functional abnormalities and diseases.

We evolve multiple curves simultaneously and represent them using signed distance functions per objects. Doing this we do not put any constraint on SDFs to

avoid intersection of evolving curves. Our joint pose prior should provide natural constraints. But, for further studies where we consider more complicated systems putting spatial constraints could be helpful to avoid collisions. However, in our experiments we do not encounter such problems.

We also mention that applying the proposed approach on other subcortical structures than CN and P can increase the help of joint pose prior. Among these topics, we are still working on 3D implementation of our current approach.

Bibliography

- [1] M. Rebates, “Available at url: <http://mrirebate.com/index.html>.”
- [2] S. S. Jasit, S. Sameer, S. K. Setarehdan, S. Rakesh, B. Keir, C. Dorin, and R. Laura, “Advanced algorithmic approaches to medical image segmentation: state-of-the-art application in cardiology, neurology, mammography and pathology,” *Springer-Verlag*, pp. 559–572, 2002.
- [3] E. Madsen and J. Gitlin, “Copper and iron disorders of the brain,” *ARN*, vol. 30, pp. 317–337, 2007.
- [4] S. D.D., B. W.G., and W. Jr. Bradley, “Magnetic resonance imaging,” *Mosby*, 1999.
- [5] A. Macovski, “Noise in mri,” *Magnetic Resonance in Medicine*, vol. 36, pp. 494–497, 1996.
- [6] S. P. Awate, T. Tasdizen, N. L. Foster, and R. T. Whitaker, “Adaptive markov modeling for mutual-information-based unsupervised mri brain-tissue classification,” *Medical Image Analysis*, vol. 10(5), p. 726739, 2006.
- [7] K. van Leemput, F. Maes, D. Vandermeulen, and P. Suetens, “A unifying framework for partial volume segmentation of brain mr images,” vol. 22, no. 1, pp. 105–119, January 2003.
- [8] I. William M. Wells, W. E. L. Grimson, R. Kikinis, and F. A. Jolesz, “Adaptive segmentation of mri data,” in *CVRMed '95*. London, UK: Springer-Verlag, 1995, pp. 59–69.
- [9] D. Mumford and J. Shah, “Boundary detection by minimizing functionals.” *CVPR*, 1985.

- [10] D. Cremers, S. J. Osher, and S. Soatto, “Kernel density estimation and intrinsic alignment for shape priors in level set segmentation,” *IJCV*, vol. 69, no. 3, pp. 335–351, 2006.
- [11] J.-P. Wang, “Stochastic relaxation on partitions with connected components and its application to image segmentation,” *Pattern Analysis and Machine Intelligence, IEEE Transactions on*, vol. 20, no. 6, pp. 619–636, 1998.
- [12] S. C. Zhu and A. Yuille, “Region competition: unifying snakes, region growing, and bayes/mdl for multiband image segmentation,” *Pattern Analysis and Machine Intelligence, IEEE Transactions on*, vol. 18, no. 9, pp. 884–900, 1996.
- [13] Y. Boykov, O. Veksler, and R. Zabih, “Fast approximate energy minimization via graph cuts,” *IEEE Trans. Pattern Anal. Mach. Intell.*, vol. 23, no. 11, pp. 1222–1239, 2001.
- [14] M. Kass, A. Witkins, and D. Terzopoulos, “Snakes: active contour models,” *International Journal Computer Vision*, vol. 1(4), pp. 321–331, 1988.
- [15] Y. Cheng, “Mean shift, mode seeking, and clustering,” *Pattern Analysis and Machine Intelligence, IEEE Transactions on*, vol. 17, no. 8, pp. 790–799, 1995.
- [16] V. Caselles, “Geometric models for active contours,” in *ICIP '95: Proceedings of the 1995 International Conference on Image Processing (Vol. 3)-Volume 3*. Washington, DC, USA: IEEE Computer Society, 1995, p. 3009.
- [17] G. Ho and P. Shi, “Domain partitioning level set surface for topology constrained multiobject segmentation,” *Biomedical Imaging: Nano to Macro, 2004. IEEE International Symposium on*, pp. 1299–1302 Vol. 2, 2004.
- [18] T. Chan and L. Vese, “Active contours without edges,” *TIP*, vol. 2, pp. 266–277, 2001.
- [19] A. Tsai, A. J. Yezzi, and A. S. Willsky, “A curve evolution approach to medical image magnification via the mumford-shah functional.” London, UK: Springer-Verlag, 2000, pp. 246–255.

- [20] J. Kim, J. W. Fisher, A. Yezzi, M. Cetin, and A. S. Willsky, “Nonparametric statistical method for image segmentation using information theory and curve evolution,” *TIP*, vol. 14, no. 10, 2005.
- [21] M. Rousson and N. Paragios, “Shape priors for level set representations,” in *ECCV '02: Proceedings of the 7th European Conference on Computer Vision-Part II*. London, UK: Springer-Verlag, 2002, pp. 78–92.
- [22] Y. Chen, H. D. Tagare, S. Thiruvankadam, F. Huang, D. Wilson, K. S. Gopinath, R. W. Briggs, and E. A. Geiser, “Using prior shapes in geometric active contours in a variational framework,” *Int. J. Comput. Vision*, vol. 50, no. 3, pp. 315–328, 2002.
- [23] F. Huang and J. Su, “Moment-based shape priors for geometric active contours.” *ICPR*, 2006, pp. 56–59.
- [24] M. Linguraru, M. Ballester, and N. Ayache, “Deformable atlases for the segmentation of internal brain nuclei in magnetic resonance imaging,” *International Journal of Computers*, vol. 2, pp. 26–36, 2007.
- [25] M. E. Leventon, W. E. L. Grimson, and O. Faugeras, “Statistical shape influence in geodesic active contours.” *CVPR*, 2000, pp. 316–323.
- [26] A. Tsai, J. Anthony Yezzi, W. W. III, C. Tempny, D. Tucker, A. Fan, W. E. Grimson, and A. Willsky, “Model-based curve evolution technique for image segmentation,” *cvpr*, vol. 1, p. 463, 2001.
- [27] Y. Chen, S. Thiruvankadam, F. Huang, K. S. Gopinath, and R. W. Brigg, “Simultaneous segmentation and registration for functional mr images,” *icpr*, vol. 01, p. 10747, 2002.
- [28] S. Jehan-Besson, M. Gastaud, M. Borland, and G. Aubert, “Region-based active contours using geometrical and statistical features for image segmentation,” *Image Processing, 2003.*, vol. 2, pp. II–643–6 vol.3, Sept. 2003.
- [29] D. Cremers, C. Schnorr, and J. Weickert, “Diffusion-snakes: Combining statistical shape knowledge and image information in a variational framework.” Washington, DC, USA: IEEE Computer Society, 2001, p. 137.

- [30] K. Gorczowski, M. Styner, J. Y. Jeong, J. S. Marron, J. Piven, H. C. Hazlett, S. M. Pizer, and G. Gerig, “Discrimination analysis using multi-object statistics of shape and pose,” *SPIE, Medical Imaging: Image Processing*, vol. 6512, March 2007.
- [31] M. N. Bossa and S. Olmos, “Statistical model of similarity transformations: Building a multi-object pose model of brain structures.” CSW-MMBIA , New York, NY, USA, June, 2006, p. 59.
- [32] J. Kim, M. Cetin, and A. S. Willsky, “Nonparametric shape priors for active contour-based image segmentation,” *SP*, vol. 87, pp. 3021 – 3044, 2007.
- [33] A. Tsai, W. Wells, C. Tempany, W. E. Grimson, and A. Willsky, “Mutual information in coupled multi-shape model for medical image segmentation,” *MIA*, vol. 8, pp. 429–445, 2004.
- [34] J. Yang, L. Staib, and J. Duncan, “Neighbor-constrained segmentation with level set based 3-d deformable models,” *Medical Imaging, IEEE Transactions on*, vol. 23, no. 8, pp. 940–948, 2004.
- [35] J. Yang and J. Duncan, “Joint prior models of neighboring objects for 3-d image segmentation.” CVPR, Washington, DC, 2004.
- [36] A. Litvin and W. C. Karl, “Coupled shape distribution-based segmentation of multiple objects.” IPMI, 2005, pp. 345–356.
- [37] C. Lu, S. M. Pizer, S. Joshi, and J.-Y. Jeong, “Statistical multi-object shape models,” *Int. J. Comput. Vision*, vol. 75, no. 3, pp. 387–404, 2007.
- [38] M. Rousson and C. Xu, “A general framework for image segmentation using ordered spatial dependency,” *MICCAI, LNCS*, vol. 4191, pp. 848–855, 2006.
- [39] M. Styner, K. Gorczowski, F. T., J. Jeong, S. Pizer, and G. Gerig, “Statistics of pose and shape in multi-object complexes using principal geodesic analysis,” *Medical Imaging and Augmented Reality*, vol. LNCS 4091, pp. 1–8, 2006.

- [40] R. J. Prokop and A. P. Reeves, “A survey of moment-based techniques for unoccluded object representation and recognition,” *CVGIP: GMIP*, vol. 54, no. 5, pp. 438–460, 1992.
- [41] S. Osher and R. Fedkiw, “Level set methods and dynamic implicit surfaces.” Springer, Berlin, 2003.
- [42] G. Slabaugh and G. Unal, “Active polyhedron: Surface evolution theory applied to deformable meshes,” 2005, pp. 84–91.
- [43] S. C. Zhu, T. S. Lee, and A. L. Yuille, “Region competition: Unifying snakes, region growing, energy/bayes/MDL for multi-band image segmentation,” in *ICCV*, 1995, pp. 416–. [Online]. Available: cite-seer.ist.psu.edu/article/zhu95region.html
- [44] S. Kichenassamy, A. Kumar, P. Olver, A. Tannenbaum, and A. Yezzi, “Gradient flows and geometric active contour models,” in *ICCV '95*, 1995, p. 810.
- [45] A. Yezzi, A. Tsai, W. Wells, C. Tempany, D. Tucker, A. Fan, W. E. Grimson, and A. Willsky, “A shape-based approach to the segmentation of medical imagery using level sets,” *TMI*, vol. 22, pp. 137–154, 2003.
- [46] G. Unal, A. Yezzi, and H. Krim, “Information-theoretic active polygons for unsupervised texture segmentation,” vol. 62, no. 3, pp. 199–220, June 2005.
- [47] T. Riklin-Raviv, N. Kiryati, and N. Sochen, “Segmentation by level sets and symmetry,” in *CVPR '06: Proceedings of the 2006 IEEE Computer Society Conference on Computer Vision and Pattern Recognition*. Washington, DC, USA: IEEE Computer Society, 2006, pp. 1015–1022.
- [48] L. Staib and J. Duncan, “Boundary finding with parametrically deformable models,” *TPAMI*, vol. 14, no. 11, pp. 1061–1075, November 1992.
- [49] A. Yezzi, A. Tsai, and A. Willsky, “A statistical approach to image segmentation for bimodal and trimodal imagery.” *ICCV*, 1999.

- [50] N. Paragios and R. Deriche, “Geodesic active contours and level sets for the detection and tracking of moving objects,” *IEEE Trans. Pattern Anal. Mach. Intell.*, vol. 22, no. 3, pp. 266–280, 2000.
- [51] A. Chakraborty, L. Staib, and J. Duncan, “Deformable boundary finding in medical images by integrating gradient and region information,” *Medical Imaging, IEEE Transactions on*, vol. 15, no. 6, pp. 859–870, 1996.
- [52] T. F. Cootes, C. J. Taylor, D. H. Cooper, and J. Graham, “Active shape models—their training and application,” *Comput. Vis. Image Underst.*, vol. 61, no. 1, pp. 38–59, 1995.
- [53] J. A. Sethian, “Level set methods and fast marching methods: Evolving interfaces in computational geometry, fluid mechanics, computer vision, and materials science.” Cambridge University Press, second edition, 1999.
- [54] D. L. Chopp, “Computing minimal surfaces via level set curvature flow,” *J. Comput. Phys.*, vol. 106, no. 1, pp. 77–91, 1993.
- [55] D. G. Kendall, “Shape manifolds, procrustean metrics and complex projective spaces,” *Bull. Lond. Math. Soc.*, vol. 16, no. 1, pp. 81–121, 1984.
- [56] C. G. Small, “The statistical theory of shapes,” *Springer-Verlag*, 1996.
- [57] R. H. Davies, T. F. Cootes, and C. J. Taylor, “A minimum description length approach to statistical shape modelling,” *Lecture Notes in Computer Science*, vol. 2082, pp. 50–??, 2001. [Online]. Available: citeseer.ist.psu.edu/davies01minimum.html
- [58] —, “A minimum description length approach to statistical shape modelling,” in *IPMI '01: Proceedings of the 17th International Conference on Information Processing in Medical Imaging*. London, UK: Springer-Verlag, 2001, pp. 50–63.
- [59] B. W. Silverman, “Density estimation for statistics and data analysis.” Chapman Hall, London, 1986.
- [60] G. Uzunbas, M. Cetin, G. Unal, and A. Ercil, “Coupled nonparametric shape priors for segmentation of multiple basal ganglia structures,” *Biomedical Imag-*

- ing: From Nano to Macro, 2008. ISBI 2008. 5th IEEE International Symposium on*, pp. 217–220, 2008.
- [61] D. Erdogmus, R. Jenssen, Y. N. Rao, and J. C. Principe, “Gaussianization: An efficient multivariate density estimation technique for statistical signal processing,” *JVLSISP*, vol. 45, pp. 67–83, 2006.
- [62] R. O. Duda, P. E. Hart, and D. G. Stork, “Pattern classification,” *Second Edition, John Willey & Sons, Inc.*, 2001.
- [63] L. Dice, “Measures of the amount of ecologic association between species,” *Ecology*, vol. 26, pp. 297–302, 1945.

Appendix A

Analytical Computation of Coupled Shape Prior Flow

We compute the gradient flow for $\log p_{\tilde{C}^1, \tilde{C}^2}(\tilde{C}^1, \tilde{C}^2)$

$$\log p_{\tilde{C}^1, \tilde{C}^2}(\tilde{C}^1, \tilde{C}^2) = \log \frac{1}{N} \sum_{i=1}^N \prod_{k=1}^2 k(d_{L_2}(\phi_{\tilde{C}^k}, \phi_{\tilde{C}_i^k}), \sigma_k) \quad (\text{A.0.1})$$

where $\phi_{\tilde{C}_i^k}$ is the signed distance function for the i th training shape for k th object. Note that $\phi_{\tilde{C}^k}$ is a function of time t and $\phi_{\tilde{C}^k}$ is a shorthand notation for the evolving level set function $\phi_{\tilde{C}^k}(t)$. Using a Gaussian kernel, we have

$$k(d_{L_2}(\phi_{\tilde{C}^k}, \phi_{\tilde{C}_i^k}), \sigma_k) = \frac{1}{\sqrt{2\pi\sigma_k^2}} \exp\left(-\frac{1}{2\sigma_k^2} \int (\phi_{\tilde{C}^k}(x) - \phi_{\tilde{C}_i^k}(x))^2 dx\right) \quad (\text{A.0.2})$$

A.1 Derivation of the Coupled Shape Prior Evolution Formula

To differentiate the expression given in (1), first we define the derivative of $\prod_{k=1}^2 k(d_{L_2}(\phi_{\tilde{C}^k}, \phi_{\tilde{C}_i^k}), \sigma_k)$. For simplicity, we will use shorthand notation k_{σ_k} for $k(d_{L_2}(\phi_{\tilde{C}^k}, \phi_{\tilde{C}_i^k}), \sigma_k)$.

$$\frac{\partial}{\partial t} k_{\sigma_1} k_{\sigma_2} = k'_{\sigma_1} k_{\sigma_2} + k_{\sigma_1} k'_{\sigma_2} \quad (\text{A.1.3})$$

$$k'_{\sigma_1} = k_{\sigma_1} \left\{ -\frac{1}{2\sigma_1^2} \int 2(\phi_{\tilde{C}^1}(x) - \phi_{\tilde{C}_i^1}(x)) \frac{\partial \phi_{\tilde{C}^1}}{\partial t}(x) \right\} \quad (\text{A.1.4})$$

$$k'_{\sigma_2} = k_{\sigma_2} \left\{ -\frac{1}{2\sigma_2^2} \int 2(\phi_{\tilde{C}^2}(x) - \phi_{\tilde{C}_i^2}(x)) \frac{\partial \phi_{\tilde{C}^2}}{\partial t}(x) \right\} \quad (\text{A.1.5})$$

Using equations (3), (4) and (5) we can define $\frac{\partial}{\partial t} \log p_{\tilde{C}^1, \tilde{C}^2}(\tilde{C}^1, \tilde{C}^2)$ as

$$\frac{\partial}{\partial t} \log p_{\tilde{C}^1, \tilde{C}^2}(\tilde{C}^1, \tilde{C}^2) = \frac{1}{p_{\tilde{C}^1, \tilde{C}^2}(\tilde{C}^1, \tilde{C}^2)} \frac{1}{N} \sum_{i=1}^N \{k'_{\sigma_1} k_{\sigma_2} + k_{\sigma_1} k'_{\sigma_2}\} \quad (\text{A.1.6})$$

$$\begin{aligned} & \frac{\partial}{\partial t} \log p_{\tilde{C}^1, \tilde{C}^2}(\tilde{C}^1, \tilde{C}^2) = \\ & \frac{1}{p_{\tilde{C}^1, \tilde{C}^2}(\tilde{C}^1, \tilde{C}^2)} \frac{1}{N} \sum_{i=1}^N \{k_{\sigma_1} k_{\sigma_2} \{-\frac{1}{2\sigma_1^2} \int 2(\phi_{\tilde{C}^1}(x) - \phi_{\tilde{C}_i^1}(x)) \frac{\partial \phi_{\tilde{C}^1}(x)}{\partial t}\} \\ & \quad + k_{\sigma_1} k_{\sigma_2} \{-\frac{1}{2\sigma_2^2} \int 2(\phi_{\tilde{C}^2}(x) - \phi_{\tilde{C}_i^2}(x)) \frac{\partial \phi_{\tilde{C}^2}(x)}{\partial t}\}\} \end{aligned} \quad (\text{A.1.7})$$

Since k_{σ_1} and k_{σ_2} are common multipliers,

$$\begin{aligned} & = \frac{1}{p_{\tilde{C}^1, \tilde{C}^2}(\tilde{C}^1, \tilde{C}^2)} \frac{1}{N} \sum_{i=1}^N k_{\sigma_1} k_{\sigma_2} \{-\frac{1}{2\sigma_1^2} \int 2(\phi_{\tilde{C}^1}(x) - \phi_{\tilde{C}_i^1}(x)) \frac{\partial \phi_{\tilde{C}^1}(x)}{\partial t}\} \\ & \quad - \frac{1}{2\sigma_2^2} \int 2(\phi_{\tilde{C}^2}(x) - \phi_{\tilde{C}_i^2}(x)) \frac{\partial \phi_{\tilde{C}^2}(x)}{\partial t}\} \end{aligned} \quad (\text{A.1.8})$$

The inner product definition;

$$\langle \phi_1, \phi_2 \rangle = \int \phi_1(x) \phi_2(x) dx \quad (\text{A.1.9})$$

Using the above definition in equation (8)

$$\begin{aligned} & \frac{\partial}{\partial t} \log (p_{\tilde{C}^1, \tilde{C}^2}(\tilde{C}^1, \tilde{C}^2)) = \\ & = \frac{1}{p_{\tilde{C}^1, \tilde{C}^2}(\tilde{C}^1, \tilde{C}^2)} \frac{1}{N} \sum_{i=1}^N k_{\sigma_1} k_{\sigma_2} \left\{ \frac{1}{\sigma_1^2} \langle \phi_{\tilde{C}_i^1}(x) - \phi_{\tilde{C}^1}(x), \frac{\partial \phi_{\tilde{C}^1}(x)}{\partial t} \rangle + \right. \\ & \quad \left. \frac{1}{\sigma_2^2} \langle \phi_{\tilde{C}_i^2}(x) - \phi_{\tilde{C}^2}(x), \frac{\partial \phi_{\tilde{C}^2}(x)}{\partial t} \rangle \right\} \end{aligned} \quad (\text{A.1.10})$$

$$\begin{aligned} & = \frac{1}{p_{\tilde{C}^1, \tilde{C}^2}(\tilde{C}^1, \tilde{C}^2)} \frac{1}{N} \sum_{i=1}^N k_{\sigma_1} k_{\sigma_2} \frac{1}{\sigma_1^2} \langle \phi_{\tilde{C}_i^1}(x) - \phi_{\tilde{C}^1}(x), \frac{\partial \phi_{\tilde{C}^1}(x)}{\partial t} \rangle + \\ & \quad \frac{1}{p_{\tilde{C}^1, \tilde{C}^2}(\tilde{C}^1, \tilde{C}^2)} \frac{1}{N} \sum_{i=1}^N k_{\sigma_1} k_{\sigma_2} \frac{1}{\sigma_2^2} \langle \phi_{\tilde{C}_i^2}(x) - \phi_{\tilde{C}^2}(x), \frac{\partial \phi_{\tilde{C}^2}(x)}{\partial t} \rangle \end{aligned} \quad (\text{A.1.11})$$

$$\begin{aligned} & = \left\langle \frac{1}{p_{\tilde{C}^1, \tilde{C}^2}(\tilde{C}^1, \tilde{C}^2)} \frac{1}{N} \sum_{i=1}^N k_{\sigma_1} k_{\sigma_2} \frac{1}{\sigma_1^2} \phi_{\tilde{C}_i^1}(x) - \phi_{\tilde{C}^1}(x), \frac{\partial \phi_{\tilde{C}^1}(x)}{\partial t} \right\rangle + \\ & \quad \left\langle \frac{1}{p_{\tilde{C}^1, \tilde{C}^2}(\tilde{C}^1, \tilde{C}^2)} \frac{1}{N} \sum_{i=1}^N k_{\sigma_1} k_{\sigma_2} \frac{1}{\sigma_2^2} \phi_{\tilde{C}_i^2}(x) - \phi_{\tilde{C}^2}(x), \frac{\partial \phi_{\tilde{C}^2}(x)}{\partial t} \right\rangle \end{aligned} \quad (\text{A.1.12})$$

We have to maximize this expression to obtain the gradient directions that increases $\log p_{\tilde{C}^1, \tilde{C}^2}(\tilde{C}^1, \tilde{C}^2)$ most rapidly for each object curve. So the gradient directions for the curves \tilde{C}^1 and \tilde{C}^2 are

$$\frac{\partial \phi_{\tilde{C}^1}}{\partial t} = \frac{1}{p_{\tilde{C}^1, \tilde{C}^2}(\tilde{C}^1, \tilde{C}^2)} \frac{1}{N} \sum_{i=1}^N k_{\sigma_1} k_{\sigma_2} \frac{1}{\sigma_1^2} (\phi_{\tilde{C}_i^1}(x) - \phi_{\tilde{C}^1}(x)) \quad (\text{A.1.13})$$

$$\frac{\partial \phi_{\tilde{C}^2}}{\partial t} = \frac{1}{p_{\tilde{C}^1, \tilde{C}^2}(\tilde{C}^1, \tilde{C}^2)} \frac{1}{N} \sum_{i=1}^N k_{\sigma_1} k_{\sigma_2} \frac{1}{\sigma_2^2} (\phi_{\tilde{C}_i^2}(x) - \phi_{\tilde{C}^2}(x)) \quad (\text{A.1.14})$$

A.2 Coupling Effect of Multiple Shapes

These final expressions for the two curves, evolve the curves toward shapes at the local maximum of objects joint shape prior, which is approximately weighted average of the neighboring training shapes of each object. Having these expressions, one can show that at the local maximum of the joint shape prior $p_{\tilde{C}^1, \tilde{C}^2}(\tilde{C}^1, \tilde{C}^2)$, the gradient flow will be zero. This means at the steady state when joint shape prior is maximum, there is no need any flow for both curves. At the steady state,

$$\begin{aligned} & \frac{\partial \phi_{\tilde{C}^k}}{\partial t} \\ &= \frac{1}{p_{\tilde{C}^1, \tilde{C}^2}(\tilde{C}^1, \tilde{C}^2)} \frac{1}{N} \sum_{i=1}^N k(d_{L_2}(\phi_{\tilde{C}^1}, \phi_{\tilde{C}_i^2}), \sigma_1) k(d_{L_2}(\phi_{\tilde{C}^2}, \phi_{\tilde{C}_i^1}), \sigma_2) \frac{1}{\sigma_1^2} (\phi_{\tilde{C}_i^k}(x) - \phi_{\tilde{C}^k}(x)) \\ &= 0 \end{aligned} \tag{A.2.15}$$

$$\frac{\partial \phi_{\tilde{C}^1}}{\partial t} = \frac{1}{\sigma_1^2} \sum_{i=1}^N \lambda_i(C^1, C^2) (\phi_{\tilde{C}_i^1}(x) - \phi_{\tilde{C}^1}(x)) = 0 \tag{A.2.16}$$

$$\frac{\partial \phi_{\tilde{C}^2}}{\partial t} = \frac{1}{\sigma_2^2} \sum_{i=1}^N \lambda_i(C^1, C^2) (\phi_{\tilde{C}_i^2}(x) - \phi_{\tilde{C}^2}(x)) = 0 \tag{A.2.17}$$

where

$$\lambda_i(C^1, C^2) = \frac{k(d_{L_2}(\phi_{\tilde{C}^1}, \phi_{\tilde{C}_i^1}), \sigma_1) k(d_{L_2}(\phi_{\tilde{C}^2}, \phi_{\tilde{C}_i^2}), \sigma_2)}{N p_{\tilde{C}^1, \tilde{C}^2}(\tilde{C}^1, \tilde{C}^2)} \text{ and}$$

$$\sum_{i=1}^N \lambda_i(C^1, C^2) = 1$$

Then the coupled shapes at the local maximum can be given as

$$\phi_{\tilde{C}^1}(x) = \frac{1}{N} \sum_{i=1}^N \lambda_i(C^1, C^2) \phi_{\tilde{C}_i^1}(x) \tag{A.2.18}$$

$$\phi_{\tilde{C}^2}(x) = \frac{1}{N} \sum_{i=1}^N \lambda_i(C^1, C^2) \phi_{\tilde{C}_i^2}(x) \tag{A.2.19}$$

Appendix B

Analytical Computation of Inter-Shape Pose Prior Flow

Definitions:

\mathcal{M} be the set of all moments.

$$M_0 = \{m_{0,0}\}$$

$$M_1 = \{m_{1,0}, m_{0,1}\}$$

$$M_n = \{m_{i,j} | m_{i,j} \in \mathcal{M}, i + j = n\}$$

$$\mathcal{M}_2 = M_0 U M_1 U M_2$$

Following Meriam - Dynamics, define the inertia moments as $I_{xx} = m_{0,2}$, $I_{xy} = I_{yx} = m_{1,1}$, and $I_{yy} = m_{2,0}$. Moreover, consider the following matrix

$$IM = \begin{pmatrix} I_{xx} & -I_{xy} \\ -I_{xy} & I_{yy} \end{pmatrix}. \quad (\text{B.0.1})$$

Let θ be the angle between the eigenvectors of IM and the axes coordinates. Then, we have

$$\theta(C) = \frac{1}{2} \arctan \left(\frac{2I_{xy}}{I_{yy} - I_{xx}} \right). \quad (\text{B.0.2})$$

Therefore,

$$\theta(C) = \frac{1}{2} \arctan \left(\frac{2(m_{1,0}m_{0,1} - m_{1,1}m_{0,0})}{(m_{0,2} - m_{2,0})m_{0,0} + m_{1,0}^2 - m_{0,1}^2} \right). \quad (\text{B.0.3})$$

B.1 Derivation of the Inter-Shape Pose Prior Evolution Formula

During the evolution of the active contour, the inter pose parameters depend on time, therefore, we have

$$\theta(C) = \frac{1}{2} \arctan \left(\frac{2(m_{1,0}(t)m_{0,1}(t) - m_{1,1}(t)m_{0,0}(t))}{(m_{0,2}(t) - m_{2,0}(t))m_{0,0}(t) + m_{1,0}^2(t) - m_{0,1}^2(t)} \right). \quad (\text{B.1.4})$$

Define

$$\text{un_sin}(2\theta) = 2(m_{1,0}(t)m_{0,1}(t) - m_{1,1}(t)m_{0,0}(t))$$

and

$$un_- \cos(2\theta) = (m_{0,2}(t) - m_{2,0}(t))m_{0,0}(t) + m_{1,0}^2(t) - m_{0,1}^2(t).$$

In addition, define $S > 0$ by $un_- \sin^2(2\theta) + un_- \cos^2(2\theta) = S^2$. Then, we can use the following interpretations: $un_- \sin(2\theta) = S \sin(2\theta)$, and $un_- \cos(2\theta) = S \cos(2\theta)$.

$$\begin{aligned} & k \left(d \left(p_{\tilde{C}^k}^{int}, p_{\tilde{C}_i^k}^{int} \right), \sigma_k \right) \\ &= \frac{1}{\sqrt{2\pi\sigma_k^2}} \exp \left\{ -\frac{1}{2\sigma_k^2} \left[\left(m_{0,0}(\tilde{C}^k) - m_{0,0}(\tilde{C}_i^k) \right)^2 + \right. \right. \\ & \quad \sum_{m_{r,s} \in \mathcal{M}_2, r+s=1} \left(\frac{m_{r,s}(\tilde{C}^k)}{m_{0,0}(\tilde{C}^k)} - \frac{m_{r,s}(\tilde{C}_i^k)}{m_{0,0}(\tilde{C}_i^k)} \right)^2 + \\ & \quad \left. \left. \left(\theta(\tilde{C}^k) - \theta(\tilde{C}_i^k) \right)^2 \right] \right\} \end{aligned}$$

In the following, we develop the derivative of the orientation angle as related to time. We use trigonometric relationships to model the moments based expressions, while keeping in mind their dependence on time. Therefore, we have

$$\begin{aligned} & \theta(C)' \\ &= \frac{1}{2} \frac{\tan'(2\theta)}{1 + \tan^2(2\theta)} \\ &= \frac{1}{2} \frac{un_- \sin'(2\theta) un_- \cos(2\theta) - un_- \sin(2\theta) un_- \cos'(2\theta)}{un_- \cos^2(2\theta) (1 + \tan^2(2\theta))} \\ &= \frac{1}{2} \frac{\left(un_- \sin'(2\theta) un_- \cos(2\theta) - un_- \sin(2\theta) un_- \cos'(2\theta) \right)}{S^2}. \\ &= \left[\left(m'_{1,0}(t) m_{0,1}(t) + m'_{0,1}(t) m_{1,0}(t) - m'_{1,1}(t) m_{0,0}(t) - m'_{0,0}(t) m_{1,1}(t) \right) \right. \\ & \quad \left. \frac{\cos(2\theta)}{S} - \left(\left(m'_{0,2}(t) - m'_{2,0}(t) \right) m_{0,0}(t) + (m_{0,2}(t) - m_{2,0}(t)) m'_{0,0}(t) \right. \right. \\ & \quad \left. \left. + 2m'_{1,0}(t) m_{1,0}(t) - 2m'_{0,1}(t) m_{0,1}(t) \right) \frac{\sin(2\theta)}{S} \right] \\ &= \left[\left(m'_{1,0} m_{0,1} + m'_{0,1} m_{1,0} - m'_{1,1} m_{0,0} - m'_{0,0} m_{1,1} \right) \frac{\cos(2\theta)}{S} - \right. \\ & \quad \left. \left(\left(m'_{0,2} - m'_{2,0} \right) m_{0,0} + (m_{0,2} - m_{2,0}) m'_{0,0} + 2m'_{1,0} m_{1,0} - 2m'_{0,1} m_{0,1} \right) \frac{\sin(2\theta)}{S} \right] \\ &= \left\{ m'_{0,0} \left[(m_{2,0} - m_{0,2}) \frac{\sin(2\theta)}{2k} - m_{1,1} \frac{\cos(2\theta)}{S} \right] + \right. \\ & \quad m'_{1,0} \left[m_{0,1} \frac{\cos(2\theta)}{S} - m_{1,0} \frac{\sin(2\theta)}{S} \right] + m'_{0,1} \left[m_{1,0} \frac{\cos(2\theta)}{S} + m_{0,1} \frac{\sin(2\theta)}{S} \right] + \\ & \quad \left. - m'_{0,2} m_{0,0} \frac{\sin(2\theta)}{2S} + m'_{2,0} m_{0,0} \frac{\sin(2\theta)}{2S} - m'_{1,1} m_{0,0} \frac{\cos(2\theta)}{S} \right\}. \tag{B.1.5} \end{aligned}$$

Define the following coefficients:

$$\begin{aligned}
M_{0,0}^\theta &= (m_{2,0} - m_{0,2}) \frac{\sin(2\theta)}{2S} - m_{1,1} \frac{\cos(2\theta)}{S} \\
M_{1,0}^\theta &= m_{0,1} \frac{\cos(2\theta)}{S} - m_{1,0} \frac{\sin(2\theta)}{S} \\
M_{0,1}^\theta &= m_{1,0} \frac{\cos(2\theta)}{S} + m_{0,1} \frac{\sin(2\theta)}{S} \\
M_{2,0}^\theta &= m_{0,0} \frac{\sin(2\theta)}{2S} \\
M_{0,2}^\theta &= -m_{0,0} \frac{\sin(2\theta)}{2S} \\
M_{1,1}^\theta &= -m_{0,0} \frac{\cos(2\theta)}{S}
\end{aligned} \tag{B.1.6}$$

Then, by substituting Equations (B.1.6) into (B.1.5), we have

$$\theta(C)' = \sum_{r=0}^2 \sum_{s=0}^{2-r} m'_{rs} M_{rs}^\theta. \tag{B.1.7}$$

$$\begin{aligned}
& k'_{\sigma_j} \\
&= k_{\sigma_j} \left\{ -\frac{1}{\sigma_j^2} \left[\left(m_{0,0}(\tilde{C}^k) - m_{0,0}(\tilde{C}_i^k) \right) \frac{\partial m_{0,0}(\tilde{C}^k)}{\partial t} + \right. \right. \\
&\quad \left. \sum_{m_{r,s} \in \mathcal{M}_{2,r+s=1}} \left(\frac{m_{r,s}(\tilde{C}^j)}{m_{0,0}(\tilde{C}^j)} - \frac{m_{r,s}(\tilde{C}_i^j)}{m_{0,0}(\tilde{C}_i^j)} \right) \frac{\partial}{\partial t} \left(\frac{m_{r,s}(\tilde{C}^j)}{m_{0,0}(\tilde{C}^j)} \right) + \right. \\
&\quad \left. \left. \left(\theta(\tilde{C}^k) - \theta(\tilde{C}_i^k) \right) \frac{\partial}{\partial t} \theta(\tilde{C}^k) \right] \right\} \\
&= k_{\sigma_j} \left\{ -\frac{1}{\sigma_j^2} \left[\left(\tilde{m}_{0,0} - \tilde{m}_{0,0}^i \right) \frac{\partial \tilde{m}_{0,0}}{\partial t} + \right. \right. \\
&\quad \left. \sum_{\tilde{m}_{r,s} \in \mathcal{M}_{2,r+s=1}} \left(\frac{\tilde{m}_{r,s}}{\tilde{m}_{0,0}} - \frac{\tilde{m}_{r,s}^i}{\tilde{m}_{0,0}^i} \right) \frac{\partial}{\partial t} \left(\frac{\tilde{m}_{r,s}}{\tilde{m}_{0,0}} \right) + \left(\tilde{\theta} - \tilde{\theta}^i \right) \frac{\partial \tilde{\theta}}{\partial t} \right] \right\} \\
&= k_{\sigma_j} \left\{ -\frac{1}{\sigma_j^2} \left[\left(\tilde{m}_{0,0} - \tilde{m}_{0,0}^i \right) \tilde{m}'_{0,0} + \right. \right. \\
&\quad \left. \sum_{\tilde{m}_{r,s} \in \mathcal{M}_{2,r+s=1}} \left(\frac{\tilde{m}_{r,s}}{\tilde{m}_{0,0}} - \frac{\tilde{m}_{r,s}^i}{\tilde{m}_{0,0}^i} \right) \left(\frac{\tilde{m}'_{r,s} \tilde{m}_{0,0} - \tilde{m}_{r,s} \tilde{m}'_{0,0}}{\tilde{m}_{0,0}^2} \right) + \right. \\
&\quad \left. \left. \left(\tilde{\theta} - \tilde{\theta}^i \right) \sum_{r=0}^2 \sum_{s=0}^{2-r} \tilde{m}'_{r,s} M_{r,s}^\theta \right] \right\} \\
&= k_{\sigma_j} \left\{ -\frac{1}{\sigma_j^2} \left[\left(\tilde{m}_{0,0} - \tilde{m}_{0,0}^i \right) \int_{\Omega} \Phi'_{\tilde{C}^j} + \right. \right. \\
&\quad \left. \sum_{\tilde{m}_{r,s} \in \mathcal{M}_{2,r+s=1}} \left(\frac{\tilde{m}_{r,s}}{\tilde{m}_{0,0}} - \frac{\tilde{m}_{r,s}^i}{\tilde{m}_{0,0}^i} \right) \left(\frac{\int_{\Omega} (x^r y^s \tilde{m}_{0,0} - \tilde{m}_{r,s}) \Phi'_{\tilde{C}^j}}{\tilde{m}_{0,0}^2} \right) \right. \\
&\quad \left. \left. \left(\tilde{\theta} - \tilde{\theta}^i \right) \sum_{r=0}^2 \sum_{s=0}^{2-r} \int_{\Omega} x^r y^s \Phi'_{\tilde{C}^j} M_{r,s}^\theta \right] \right\} \\
&= k_{\sigma_j} \left\{ -\frac{1}{\sigma_j^2} \left[\left(\tilde{m}_{0,0} - \tilde{m}_{0,0}^i \right) \langle 1, \Phi'_{\tilde{C}^j} \rangle + \right. \right. \\
&\quad \left. \sum_{\tilde{m}_{r,s} \in \mathcal{M}_{2,r+s=1}} \left(\frac{\tilde{m}_{r,s}}{\tilde{m}_{0,0}} - \frac{\tilde{m}_{r,s}^i}{\tilde{m}_{0,0}^i} \right) \left\langle \frac{(x^r y^s \tilde{m}_{0,0} - \tilde{m}_{r,s})}{\tilde{m}_{0,0}^2}, \Phi'_{\tilde{C}^j} \right\rangle \right. \\
&\quad \left. \left. \left(\tilde{\theta} - \tilde{\theta}^i \right) \sum_{r=0}^2 \sum_{s=0}^{2-r} \langle x^r y^s M_{r,s}^\theta, \Phi'_{\tilde{C}^j} \rangle \right] \right\} \\
&= k_{\sigma_j} \left\{ \left\langle -\frac{1}{\sigma_j^2} \left[\left(\tilde{m}_{0,0} - \tilde{m}_{0,0}^i \right) + \right. \right. \right. \\
&\quad \left. \sum_{\tilde{m}_{r,s} \in \mathcal{M}_{2,r+s=1}} \left(\frac{\tilde{m}_{r,s}}{\tilde{m}_{0,0}} - \frac{\tilde{m}_{r,s}^i}{\tilde{m}_{0,0}^i} \right) \frac{(x^r y^s \tilde{m}_{0,0} - \tilde{m}_{r,s})}{\tilde{m}_{0,0}^2} + \right. \\
&\quad \left. \left. \left. \left(\tilde{\theta} - \tilde{\theta}^i \right) \sum_{r=0}^2 \sum_{s=0}^{2-r} x^r y^s M_{r,s}^\theta \right], \Phi'_{\tilde{C}^j} \right\rangle \right\}
\end{aligned}$$

Define the moments speed factor (MSP) of the object o in $\{NC, P\}$ as

$$\begin{aligned}
MSF(o) &= (\tilde{m}_{0,0} - \tilde{m}_{0,0}^i) + \\
&\quad \sum_{m_{r,s} \in \mathcal{M}_{2,r+s=1}} \left(\frac{\tilde{m}_{r,s}}{\tilde{m}_{0,0}} - \frac{\tilde{m}_{r,s}^i}{\tilde{m}_{0,0}^i} \right) \frac{(x^r y^s \tilde{m}_{0,0} - \tilde{m}_{r,s})}{\tilde{m}_{0,0}^2} + \\
&\quad (\tilde{\theta} - \tilde{\theta}^i) \sum_{r=0}^2 \sum_{s=0}^{2-r} x^r y^s M_{r,s}^\theta
\end{aligned} \tag{B.1.8}$$

$$\begin{aligned}
&\frac{\partial}{\partial t} \log P_p(\tilde{\mathbf{C}})(p_{int}|\tilde{\mathbf{C}}) \\
&= \left\langle \frac{\sum_{i=1}^N \frac{k_{\sigma_1} k_{\sigma_2}}{-\sigma_1^2} MSF(1)}{P_p(\tilde{\mathbf{C}})(p_{int}|\tilde{\mathbf{C}}) \cdot N}, \frac{\partial \Phi_{\tilde{\mathbf{C}}^1}}{\partial t} \right\rangle + \left\langle \frac{\sum_{i=1}^N \frac{k_{\sigma_1} k_{\sigma_2}}{-\sigma_2^2} MSF(2)}{P_p(\tilde{\mathbf{C}})(p_{int}|\tilde{\mathbf{C}}) \cdot N}, \frac{\partial \Phi_{\tilde{\mathbf{C}}^2}}{\partial t} \right\rangle
\end{aligned} \tag{B.1.9}$$

$$\begin{aligned}
\frac{\partial \Phi_{\tilde{\mathbf{C}}^1}}{\partial t}(x, y) &= \frac{\sum_{i=1}^N \frac{k_{\sigma_1} k_{\sigma_2}}{-\sigma_1^2} MSF(1)}{P_p(\tilde{\mathbf{C}})(p_{int}|\tilde{\mathbf{C}}) \cdot N} \\
\frac{\partial \Phi_{\tilde{\mathbf{C}}^2}}{\partial t}(x, y) &= \frac{\sum_{i=1}^N \frac{k_{\sigma_1} k_{\sigma_2}}{-\sigma_2^2} MSF(2)}{P_p(\tilde{\mathbf{C}})(p_{int}|\tilde{\mathbf{C}}) \cdot N}
\end{aligned}$$